ACS APPLIED NANO MATERIALS

Open Access

www.acsanm.org

Article

Metal-Free Multilayer Graphene Electrodes Activated by PECVD for Electrochemical Oxidation Enhancement

Tarso Leandro Bastos, Camila Cristina da Silva, Daniela Nunes, Elvira Fortunato, Rodrigo Martins, Devadharshini Kathan, William Earl Mustain, Jr, Rogério Valentim Gelamo, and Flavio Colmati*

Cite This: *ACS Appl. Nano Mater.* 2025, 8, 22586−22604

Read Online

ACCESS | Metrics & More | Article Recommendations | Supporting Information

ABSTRACT: Multilayer graphene (MLG) was obtained by 3 h ultrasonication of thermally expanded graphite in *n*-propanol, producing 5−13-nm-thick flakes with 1−50 μm lateral size. The powder was dry-pressed into self-supported disk electrodes (MLGD) and surface-activated by brief MW-PECVD and RF-PECVD in Ar/CO_2 and Ar/O_2. PECVD raised Raman I_D/I_G from 0.07 to 0.26−0.28 ($L_a \approx 275 \rightarrow 69-92$ nm) and gave higher localized O for CO_2 MW-PECVD (≈1.05 wt % vs ≈0.13 wt % for O_2). Electrochemically, areal capacitance increased ≈11.9 → ≈16.5 mF·cm^{-2} (∼39%), and ethanol oxidation peak currents improved up to ≈ 40% (peak up to 2.94 mA·cm^{-2} for O_2 RF-PECVD in 1.0 M NaOH + 2.0 M EtOH), with >95% capacitance retention after 15 CV cycles. These results highlight that PECVD post-treatment provides a rapid, reagent-free, and tunable surface functionalization of compacted MLG electrodes, enabling increased capacitance and enhanced ethanol oxidation with minimal bulk structural degradation.

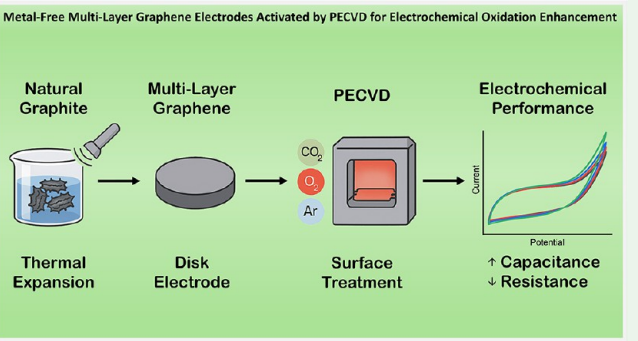

KEYWORDS: *Ar/CO_2 and Ar/O_2 glow discharges, ethanol oxidation, PECVD, plasma process, surface functionalization*

INTRODUCTION

Highlighted as one of the most versatile materials, graphene has attracted significant attention for its electrochemical properties and broad applications, while its production methods still face challenges.[1,2] Despite advances in the synthesis using mechanical cleavage, liquid-phase exfoliation, chemical vapor deposition (CVD), Hummers' methods, and gas-phase synthesis, graphene production lacks a scalable option that simultaneously provides high yield and high purity.[3−5] In response, recent work has explored hybrid strategies that combine bulk exfoliation with postsynthesis surface engineering in order to bridge the gap between quantity and quality. In this context, plasma-based techniques have emerged as powerful tools both for low-temperature growth and for precise surface functionalization; plasma-enhanced chemical vapor deposition (PECVD) is among the most widely reported of these methods.[6]

Plasma treatment techniques are now widely used in both academic laboratories and industry for surface modification and functionalization.[7] PECVD assisted by microwave (MW) or radiofrequency (RF) excitation can introduce controlled defects and oxygenated (or other heteroatom) functional groups and tune the sp^2/sp^3 ratio on graphene surfaces, thereby modulating the material's electronic and chemical properties.[8] Compared with wet chemical routes, plasma processing avoids solvent contamination and hazardous reagents; moreover, unlike aggressive chemical oxidation that often lacks fine control, PECVD allows rapid, gas-phase tuning of defect density and chemistry.[9,10] While PECVD setups require vacuum chambers and controlled gas feeds, they can yield films and functionalized surfaces with excellent crystallinity control, reproducibility, and, when properly optimized, lower defect densities than aggressive wet chemistries, the attributes that make PECVD attractive when electrical performance and patterning precision are required.[11,12]

Beyond growth, plasma treatments can be applied as a postprocessing route to selectively activate surfaces: they promote controlled edge defects and holes, modify layer edges, and graft oxygen-containing groups that improve electrolyte wetting and facilitate charge transfer at the electrode−electrolyte interface.[13,14] In particular, introducing edge sites and oxygenated groups mitigates problems such as restacking and hydrophobicity by interrupting van der Waals interactions and increasing the density of electrochemically active sites.[15]

Received: August 1, 2025
Revised: October 29, 2025
Accepted: October 30, 2025
Published: November 18, 2025

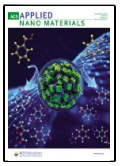

Surface doping and functionalization therefore provide practical levers to tune the electrochemical behavior (capacitance, charge transfer, and catalytic activity) without wholesale loss of the sp^2 network.[16−18]

Graphene-based electrodes are attractive for energy applications by virtue of high electrical conductivity, large specific surface area, chemical stability, and low mass.[19] When used as catalyst supports or binder-free electrodes, graphene materials can enhance electrochemical reactions; for instance, graphene-supported catalysts have been reported to show pronounced ethanol oxidation peaks in alkaline media due to enhanced OH^--mediated surface reactions.[20] Likewise, plasma surface modification has been shown to control not only capacitance but also catalyst−support interactions and alloy binding, offering routes to tune electrode performance for fuel cells and electrochemical energy storage.[21,22]

In light of the increasing demand for high-performance, scalable electrode materials for energy storage and conversion (portable electronics, hybrid vehicles, and stationary power), methods that combine bulk production with rapid, clean surface activation are of high practical interest.[23,24] Here, we present a combined strategy that addresses these needs: (i) a scalable, high-throughput exfoliation route to produce multilayer graphene (MLG) from thermally expanded natural graphite, yielding large lateral-size flakes with low baseline defect density suitable for electrode fabrication and (ii) a rapid, solvent-free PECVD post-treatment (MW or RF, with Ar/CO_2 or Ar/O_2 feeds) applied to compacted, self-supported MLG disk electrodes to introduce controlled edge defects and oxygen functionalities. This integrated approach merges the yield advantages of bulk exfoliation with the precision of plasma surface engineering, enabling tunable enhancement of capacitance and ethanol oxidation activity while maintaining bulk crystallinity, minimal contamination, and good electrical connectivity.

EXPERIMENTAL SECTION

Preparation of Multilayer Graphene (MLG). The MLG sheets were prepared from thermally expanded natural graphite flakes donated by Nacional de Grafite Ltda. To exfoliate the graphite powder and obtain an MLG dispersion, a mechanical process by ultrasound with propanol was performed for 3 h, as previously investigated by our group producing multilayer graphene powder (GP).[25,26] Disk electrodes (MLGD) were then fabricated by compaction of 60 mg of GP in a stainless steel cylindrical mold (3.0 cm diameter) for 1 min in a hydraulic press under a constant pressure of 250 kgf/cm^2.

PECVD was employed as a post-treatment step to functionalize the surface of the already-compacted MLGD electrodes. Selected MLGD samples were treated by microwave-assisted plasma-enhanced chemical vapor deposition (MW-PECVD) at a frequency of 2.42 GHz through a 1000 W magnetron (LG Co.), which has been described in detail previously.[1,26] The reactive cold plasma discharges were obtained by using mixtures of Ar (3.5×10^{-2} Torr) in two different atmospheres individually: CO_2 (3.5×10^{-2} Torr) and O_2 (3.5×10^{-2} Torr) controlled by needle valves for 2 min.[27] A second post-treatment that consisted by a radiofrequency-assisted plasma-enhanced chemical vapor deposition (RF-PECVD) was done in an O_2 atmosphere and was used for MLGD treatment.[28] In the RF-PECVD setup, the plasma is generated between two horizontal parallel-plate electrodes, in a stainless steel vacuum chamber fed by a radio-frequency (300 W) power generator purchased from RFVII Co connected directly to the impedance matching network. The chamber was evacuated by a rotative pump RV12 (Edwards Co) and pressurized with a mix of Ar (5.4×10^{-1} Torr) and O_2 (0.6×10^{-1} Torr), applying power of 65 W for 25 min on each sample side.

Effect of Exfoliation Parameters on Flake Properties. Key experimental parameters that govern the resulting MLG morphology are solvent selection, sonication energy/intensity, sonication time, dispersion concentration, and temperature control. Solvents with surface energies close to that of graphene (e.g., certain alcohols and dipolar aprotic solvents) facilitate exfoliation and stabilization of few-layer flakes. Increased sonication energy and longer sonication times generally improve the exfoliation yield and produce thinner flakes but at the expense of increased edge defects and some in-plane disorder (higher I_D/I_G in Raman). Probe (tip) sonication typically produces higher shear forces and faster exfoliation than bath sonication, resulting in smaller lateral sizes but more defects if overprocessed. Likewise, elevated temperature during sonication accelerates exfoliation but can promote reaggregation or chemical attack; for this reason, we used intermittent cooling. In our samples (3 h sonication in *n*-propanol), we observe flakes with thickness in the 5−13 nm range and lateral size predominantly 15−50 μm (TEM/SEM/ImageJ measurement; see Results and Discussion section and Supporting Information (SI)). Raman spectra and TEM indicate minimal basal-plane damage under the chosen conditions, consistent with a high-yield, low-defect multilayer product optimized for electrode fabrication.[3,25]

Physical Characterization. After their preparation, compositional analyses were performed using energy-dispersive X-ray spectroscopy (EDS), with an Oxford Instruments XMax-n 80 X-ray detector coupled to the microscope. The images were obtained by using a Jeol JSM7100F field-emission scanning electron microscope (FEG-SEM) with an electron acceleration voltage of 5 kV in secondary electron detection (SED) mode. Secondary (SE) and bright-field (BF) scanning transmission electron microscopy (STEM) observations were conducted using a Hitachi HF5000 probe-corrected field-emission transmission electron microscope operating at 200 kV. A drop of the sonicated dispersion of each powder was applied to lacey-carbon copper grids and left to dry prior to observation. Subsequently, ImageJ software was used to measure the size of the analyzed material.

X-ray diffraction was performed using a Shimadzu diffractometer model DRX-6000, depositing the powder samples of the electrocatalysts on the glass support, using an incident angle of 10−90° and scanning speed of 2°/min with an incident radiation wavelength of 1.54 Å (Cu K at 40 kV and 30 mA) at a temperature of 23 °C.

Raman mapping was acquired with a Renishaw in Via (07UM05) using a 532 nm laser and a 1800 l·mm^{-1} grating with a 100× objective. Maps comprised 900 points per sample (5 spectra averaged per point), exposure of 0.5 s per point, and 5% laser power. The D and G peak areas were integrated to obtain I_D/I_G (area), and crystallite sizes (L_a) were estimated using the Cançado relation appropriate for low-to-moderate defect densities (Ferrari−Robertson Stage 1).[29]

Cyclic Voltammetry Testing. Electrochemical characterizations were performed in a three-electrode electrochemical cell with a (Pt)-gauze counter electrode and $Ag/AgCl/KCl_{sat}$ as the reference electrode for acid medium, and the saturated calomel electrode (SCE) was used as reference for the alkaline medium. The measurements were carried out with an Autolab PGSTAT 302N potentiostat/galvanostat at room temperature (~27 °C) in 0.5 M H_2SO_4 (Sigma-Aldrich) and 1.0 M NaOH (Sigma-Aldrich) both with four ethanol concentrations in the electrolyte. The working electrode was prepared by depositing a 35 μL aliquot of ink into a Teflon-shrouded 0.385 cm^2 glassy-carbon disk electrode. The ink composition was as follows: 5 mg of GP, 1.4 mL of water, 1.0 mL of ethanol, and 0.1 mL of Nafion 117 solution (Sigma-Aldrich). A Teflon-shrouded (Au)-gauze electrode (geometric area is 0.7854 cm^2) was used as an electrical contact support to the MLGD electrodes, tested by complete immersion in the three-electrode cell solution.

The calculation formulas and normalization procedure are provided here for reproducibility. Specific capacitance (mF/mg) was calculated from the CV curves as

https://doi.org/10.1021/acsanm.5c03602
ACS Appl. Nano Mater. 2025, 8, 22586−22604

$$C_{mass} = \frac{\int I(V)dV}{v \cdot \Delta V \cdot m}$$

where m is the mass of GP deposited (determined from suspension concentration and deposited volume and confirmed gravimetrically). Areal capacitance (mF/cm^2) was calculated as

$$C_{area} = \frac{\int I(V)dV}{v \cdot \Delta V \cdot A}$$

where A is the electrode geometric area. Both normalizations are reported in the paper (Tables 1 and 2) to allow material-level and electrode-level comparisons.

Table 1. Capacitances of GP Electrodes Calculated from Figure 8

	capacitance (mF/mg)		capacitance (mF/cm^2)	
electrode	acid	alkaline	acid	alkaline
graphene	3.5	1.8	0.64	0.33
ethanol 0.5 M	3.2	1.9	0.58	0.35
ethanol 1.0 M	2.9	2.1	0.53	0.38
ethanol 2.0 M	2.6	2.0	0.48	0.36
ethanol 3.0 M	2.4	1.9	0.44	0.34

Table 2. Capacitances and Current Peaks of MGLD Electrodes Obtained from Figure 9

	capacitance (mF/cm^2)		current peak (mA/cm^2)	
electrode	acid	alkaline	acid	alkaline
Electrolyte				
MLGD pristine	11.88	9.10	1.01	0.70
MLGD-CO_2 MW-PECVD	16.15	10.03	1.39	0.81
MLGD-O_2 MW-PECVD	16.52	10.40	1.34	0.76
MLGD-O_2 RF-PECVD	15.98	11.54	1.36	0.88
Electrolyte + 2.0 M Ethanol				
MLGD pristine	12.48	8.85	1.14	2.09
MLGD-CO_2 MW-PECVD	16.58	8.92	1.50	2.31
MLGD-O_2 MW-PECVD	16.76	9.53	1.47	2.52
MLGD-O_2 RF-PECVD	15.46	9.95	1.46	2.94

To evaluate the catalytic performance of MLGD, we chose ethanol oxidation as the model reaction. Ethanol is widely used as a benchmark fuel in direct alcohol fuel cell and electrocatalysis studies because it is readily soluble in aqueous electrolytes and, when completely oxidized, can deliver up to 12 electrons per molecule, providing a high theoretical charge yield. Additionally, ethanol exhibits lower membrane crossover and fewer contamination issues than methanol in practical fuel cell contexts, and therefore provides a safer and more representative liquid fuel for comparative electrode testing.[30,31] We also evaluated H_2 feeding in a three-electrode aqueous cell, but direct hydrogen bubbling generated significant bubble-induced noise and unstable contact at the electrode−electrolyte interface, producing data with insufficient reproducibility for the present comparative study. For these practical and mechanistic reasons, controlled ethanol solutions in a three-electrode cell were chosen as the most suitable platform to isolate and quantify the effects of PECVD-modified MLG disk electrodes.

Electrochemical impedance spectroscopy measurements were performed by using an AUTOLAB PGSTAT 302N potentiostat. Data acquisition was carried out with NOVA 2.1.7 software, and data treatment and fitting were performed with AfterMath Electrochemical Studio. The measurements were conducted in a conventional three-electrode cell, employing the MLGD electrode as the working electrode, a Pt wire as the counter electrode, and an Ag/AgCl/KCl_{sat} electrode as reference. The electrolyte consisted of a 0.1 M KOH solution. The impedance spectra were recorded at a fixed potential of 0.1 V vs Ag/AgCl, with a frequency range from 50 kHz to 1 mHz, applying a sinusoidal AC perturbation of 1 mV (p−p). All measurements were carried out at ambient temperature (approximately 20 °C). EIS fittings used constant phase elements (CPE) to model nonideal capacitive behavior. CPE parameters Y_0 and n were converted to effective capacitance (C_{eff}) using the approach described by Hirschorn et al. to enable direct comparison with CV-derived capacitances.[32]

RESULTS AND DISCUSSION

Along with the highlighted new materials researched in the past decades, graphene is promising, but in the meantime it struggles with the scalability of production. The major issues are linked with quality control, purity, and cost of equipment and processes. The individual MLG sheets exhibit lateral dimensions of 1−50 μm and thicknesses of 5−13 nm, as determined from the SEM/TEM analysis, without the characteristic grain boundaries observed in polycrystalline graphene produced by CVD methods. These dimensions are consistent with the moderate-energy ultrasonication protocol employed here (3 h in n-propanol) (Figure 1), which promotes efficient exfoliation of expanded graphite while largely preserving the basal-plane order. In general, longer sonication times or higher probe powers tend to reduce the lateral size and increase disorder, leading to a higher D/G intensity ratio in Raman spectra.[25] The balance observed in our samples therefore reflects a compromise between exfoliation yield and defect generation, yielding multilayer graphene with a large lateral size and relatively low defect density suitable for electrode fabrication. The graphene sheets exhibit strong intermolecular interactions that could, in principle, lead to stacking. However, in our samples, such stacking was minimal, likely due to the small sheet thickness and synthesis conditions. These strong interactions simultaneously facilitate a high degree of anchoring for metal nanoparticles, ensuring a high metal loading and uniform dispersion on the graphene surface.[33,34] Figure 2c,d shows SEM images of the synthesized multilayer graphene powder (MLG) after thermal expansion, in comparison with the pristine natural graphite precursor. The expanded MLG exhibits thinner, well-separated sheets with higher structural uniformity and reduced layer stacking, whereas the original graphite (Figure 2a,b) displays thick, densely packed lamellae characteristic of the bulk material. These observations confirm the efficiency of the thermal expansion step in promoting interlayer separation and partial exfoliation, yielding a more open morphology favorable for subsequent PECVD functionalization.[35] These features enable the electrochemical application of MLGD avoiding the intrinsics disadvantages, while maintaining the benefits, such as, high surface area, high electrical conductivity, porosity, and adsorption resistance to some chemical species.[36,37]

Figure 3 presents the X-ray diffraction patterns of multilayer graphene powder (GP) and the MLG disk electrodes (MLGD). The present peaks at 27° and 54° in 2θ are assigned to Miller indices of C (002) and C (004), where the sharp narrow shape indicates the crystallinity of the graphene structure. The peaks around 42°, 44°, 77°, and 87°, Miller indices of C (100), C (101), C (110), and C (006), respectively, can be assigned to the crystal structure of graphite.[38,39] These results, along with EDS (Figure 5), demonstrate the purity of graphene synthesized by our method, conversely to residues and contamination on graphene obtained by liquid-phase exfoliation, reduction of

https://doi.org/10.1021/acsanm.5c03602
ACS Appl. Nano Mater. 2025, 8, 22586−22604

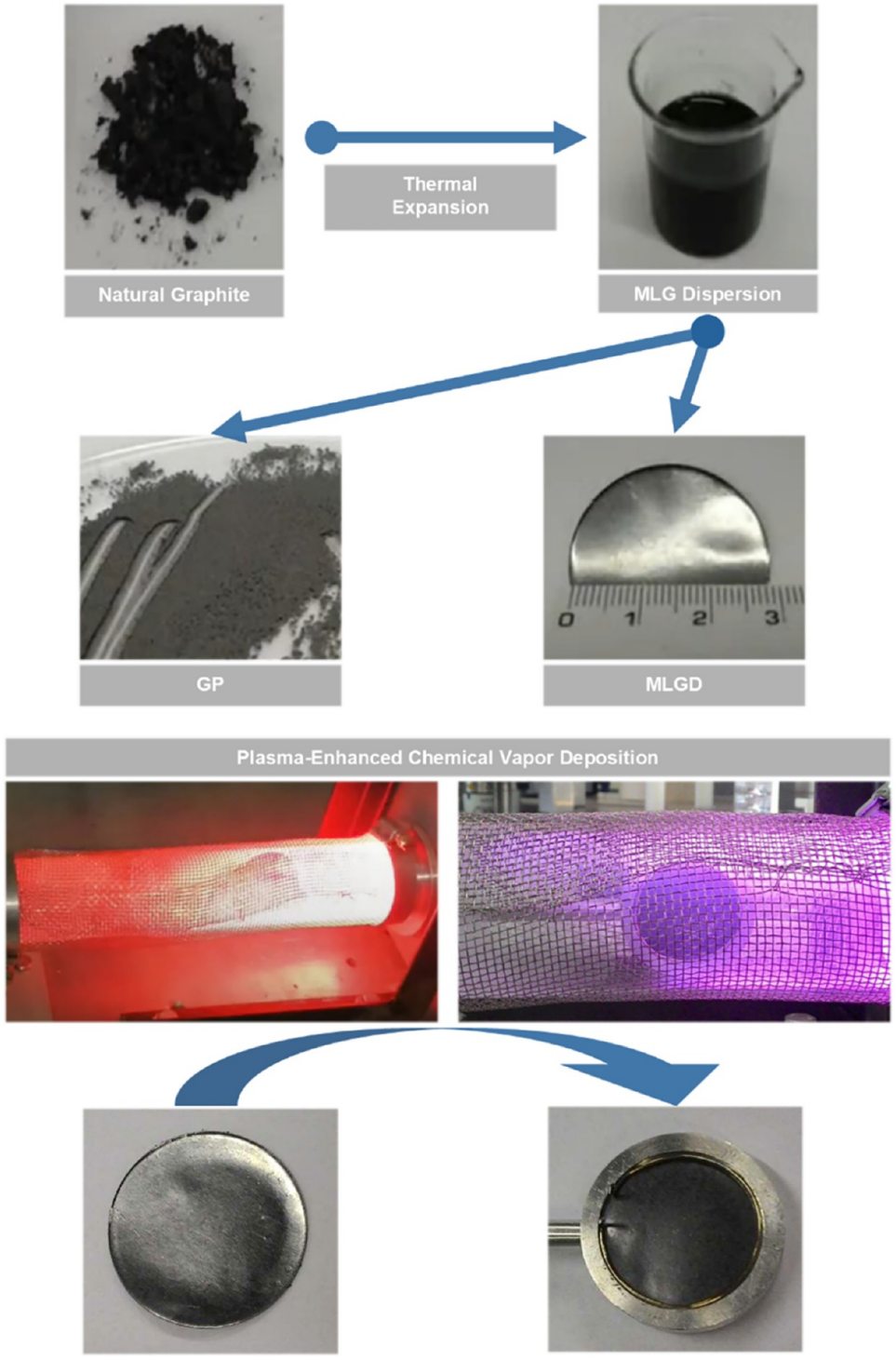

Figure 1. Schematic diagrams of the synthesis processes and PECVD treatment.

graphene oxides, and epitaxial growth on silicon carbide (SiC) methods. At the same time, elemental mapping indicates a certain amount of oxygen species on the graphene surface of MLGD-CO_2 MW-PECVD than MLGD-O_2 MW-PECVD, corroborating with the more intense surface change shown by SEM images. Figure 3 presents two spectra, GP and MLGD, and thus an issue related to physical modifications or sample preparations is the change in the original properties; in this case, the manufacturing compacting of graphene powder in a disk could alter their physical structure. Nonetheless, the absence of some peaks in MLGD in comparison with GP is due to the flake orientation by the compression process, which increased the sharp peaks of C (002), C (004), and C (006), obscuring the view of the other peaks. Despite that, the peaks alignment between them establishes the same crystalline features; therefore, all electrochemical data of both GP and MLGD can be analyzed together.

The C(002) reflection of the compacted MLGD disks exhibits a small left-hand shoulder (lower 2θ) and an asymmetric profile relative to the GP powder. Such asymmetry

https://doi.org/10.1021/acsanm.5c03602
ACS Appl. Nano Mater. 2025, 8, 22586−22604

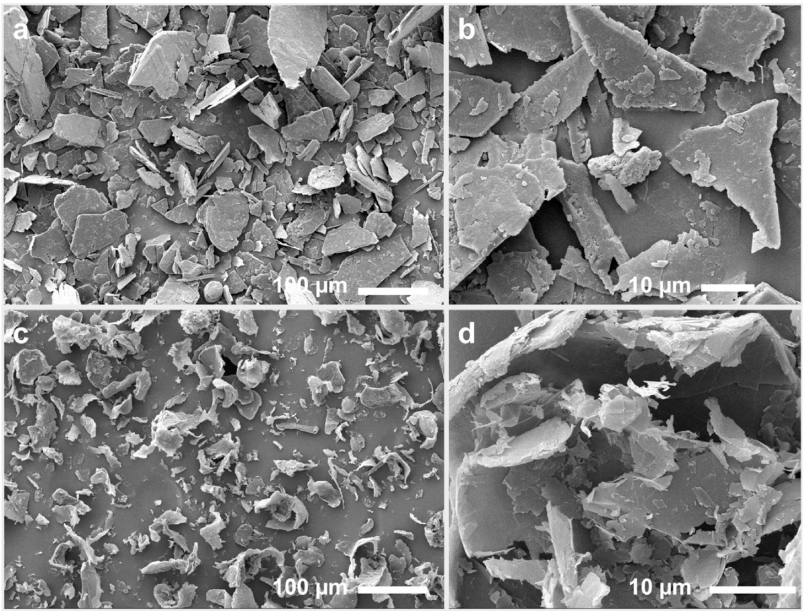

Figure 2. SEM of (a, b) natural graphite and (c, d) multilayer graphene powder (GP).

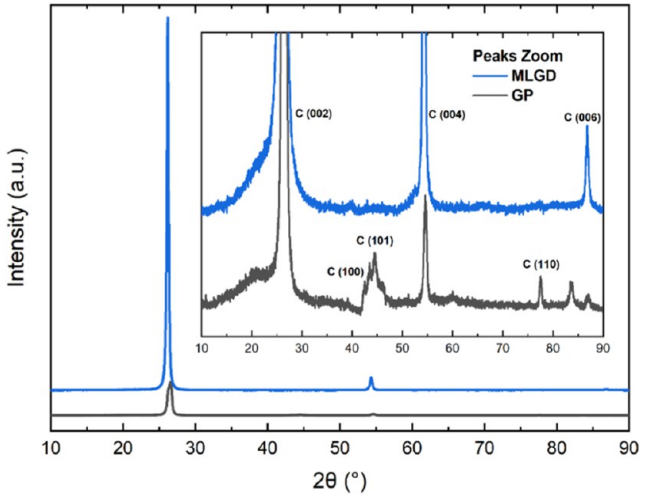

Figure 3. XRD of GP (black) pristine powder from synthesis and disk electrodes MLGD (blue).

of the (00l) family is well-documented for graphitic materials and may arise from turbostratic stacking (rotational and translational disorder between graphene layers), local variation of interlayer spacing, and preferred orientation (texture) introduced by the mechanical compaction process rather than from an additional crystalline impurity. Warren's random-layer lattice theory and subsequent simulations show that stacking disorder and layer rotation generate asymmetric and broadened (00l) features; numerical modeling further demonstrates how fluctuations in d(002) and curvature produce shoulders at lower 2θ.[40,41] Moreover, oxidation/intercalation or small populations of less-ordered graphenic domains produce an effective increase in interlayer spacing and a broad low-angle contribution beneath the main (002) peak, which appears as a left shoulder in the measured pattern.[42,43] In our samples, no additional diffraction lines attributable to foreign crystalline phases are observed, and elemental mapping/EDS (Figure 5) does not indicate significant contamination; therefore, we attribute the observed asymmetry primarily to turbostratic disorder and compaction-induced texture.

Figure 4 presents Raman results and consists of 2D maps for all samples herein studied. The averages of the 900 spectra of each sample studied that resulted in the 2D maps are also presented. The averaged Raman metrics for the samples are pristine MLG (I_D/I_G = 0.07, $L_a \approx$ 275 nm), CO_2 MW-PECVD (I_D/I_G = 0.28, $L_a \approx$ 69 nm), O_2 MW-PECVD (I_D/I_G = 0.26, $L_a \approx$ 74 nm), and O_2 RF-PECVD (I_D/I_G = 0.21, $L_a \approx$ 92 nm). These values confirm that PECVD treatments move the compacted MLG along the Stage-1 amorphization trajectory—i.e., increased I_D/I_G corresponds to smaller sp^2 domain sizes and higher density of edge/point defects, while the G-band remains dominated by sp^2 vibrations, consistent with retention of a largely conjugated network.[29] Although it may seem counterintuitive that a CO_2 feedstock yields higher oxygen incorporation than molecular O_2, the plasma chemistry and dissociation pathways explain this observation. CO_2 plasmas generate a mixture of reactive species (CO, CO*, O, OH, CxOy radicals) and intermediate carbon−oxygen fragments that can graft oxygen functional groups (C−O, C═O) onto near-surface carbon while simultaneously creating defects; in contrast, energetic O_2 plasmas tend to favor oxidative etching and removal of carbon atoms, which can leave less residual surface oxygen in some regimes. Empirical plasma functionalization studies on graphite/graphene systems have observed similar trends, with CO_2 discharges introducing abundant oxygenated groups, while O_2 discharges under aggressive conditions produce stronger etching/fragmentation. Our measured higher I_D/I_G for CO_2 MW-PECVD is therefore consistent with a CO_2-driven pathway that both functionalizes and defects the surface rather than simply removing the material.

Microwave (MW) and radiofrequency (RF) plasmas differ in their power coupling, electron energy distributions, and plasma densities. MW plasmas commonly produce higher localized electron energy and higher radical densities at comparable nominal power, leading to faster reaction kinetics on the surface (both functionalization and etching). RF

https://doi.org/10.1021/acsanm.5c03602
ACS Appl. Nano Mater. 2025, 8, 22586−22604

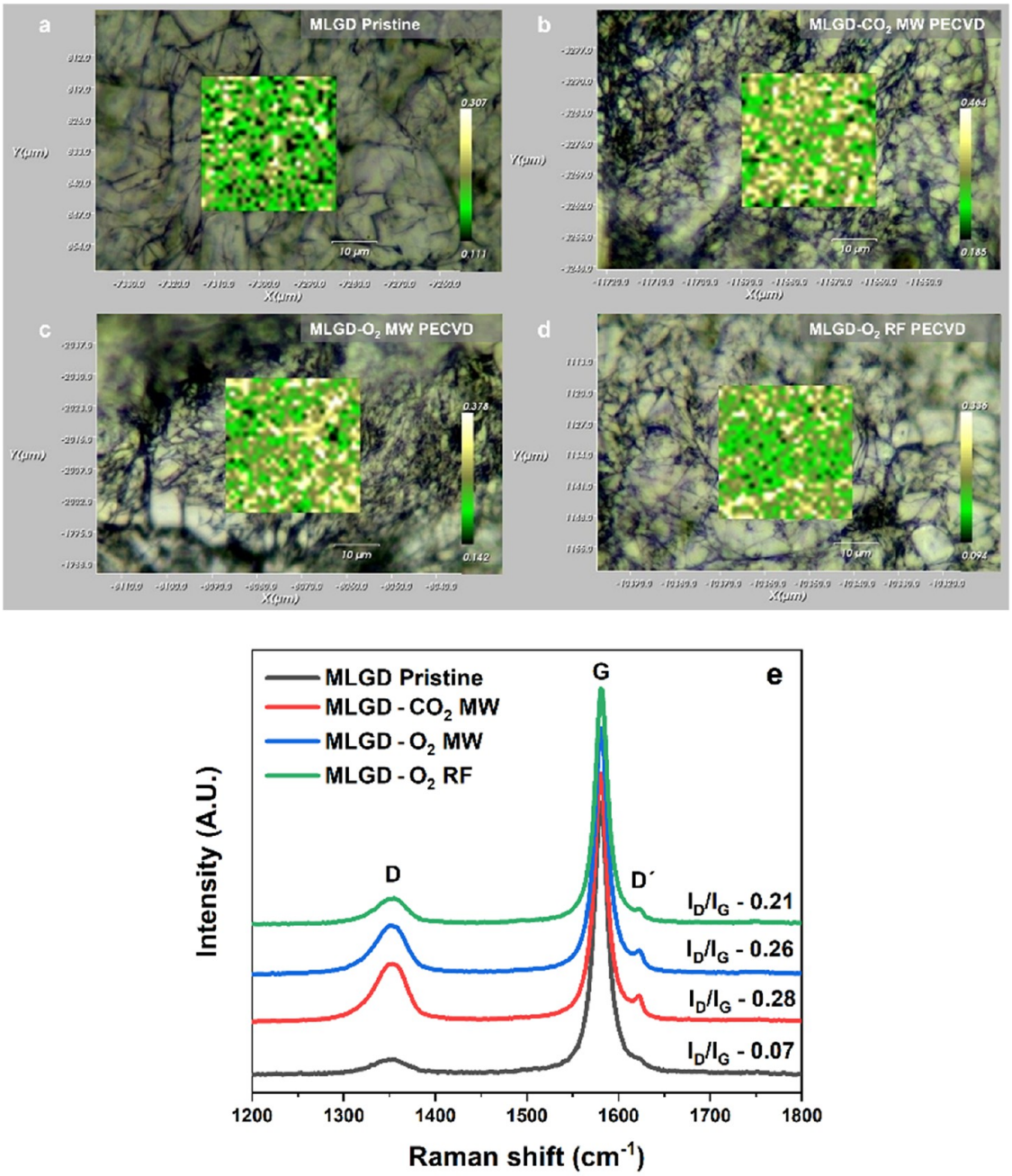

Figure 4. Raman maps of I_D/I_G ratios of (a) MLGD pristine, (b) MLGD-CO_2 MW-PECVD, (c) MLGD-O_2 MW-PECVD, (d) MLGD-O_2 RF-PECVD, and (e) Raman spectrum.

discharges typically produce more uniform, lower-energy plasmas with gentler modification. These mechanistic differences rationalize why MW treatments (CO_2 or O_2) yield the highest I_D/I_G values in our data set, while RF-PECVD (O_2) produces a more moderate increase in I_D/I_G together with larger L_a, a combination that preserves conductivity while introducing useful active sites.[44] In Stage-1 materials, an increased I_D/I_G (smaller L_a) signals a larger population of edges, vacancies, and oxygenated defects that introduce localized states in the electronic density of states (DOS) near the Fermi level. These localized states can shift/reshape the effective DOS at Ef, increase electronic localization at defect sites, and modify the local work function. Practically, a moderate increase in defectivity and oxygen functionalization can raise the density of active sites for adsorption and charge transfer without rendering the material insulating; an excessive defect concentration, however, will reduce percolative conduction and degrade kinetics. Raman alone does not give direct chemical speciation (types of oxygen groups) or depth profiling, but the I_D/I_G + L_a trends are consistent with an increased near-surface population of reactive centers able to interact with the electrolyte species.[45]

The plasma-enhanced chemical vapor deposition (PECVD) is a treatment also used to modify the surface structure that, combined with the appropriate choice of gases and its partial pressures, can promote the formation of functional groups as well as alter the electronic properties of the samples by reactive species present in the glow discharge, such as, electrons, ions, and free radicals.[46] In the case of graphene, this can be used to generate defects on the surface and edge of the layers, enabling

https://doi.org/10.1021/acsanm.5c03602
ACS Appl. Nano Mater. 2025, 8, 22586−22604

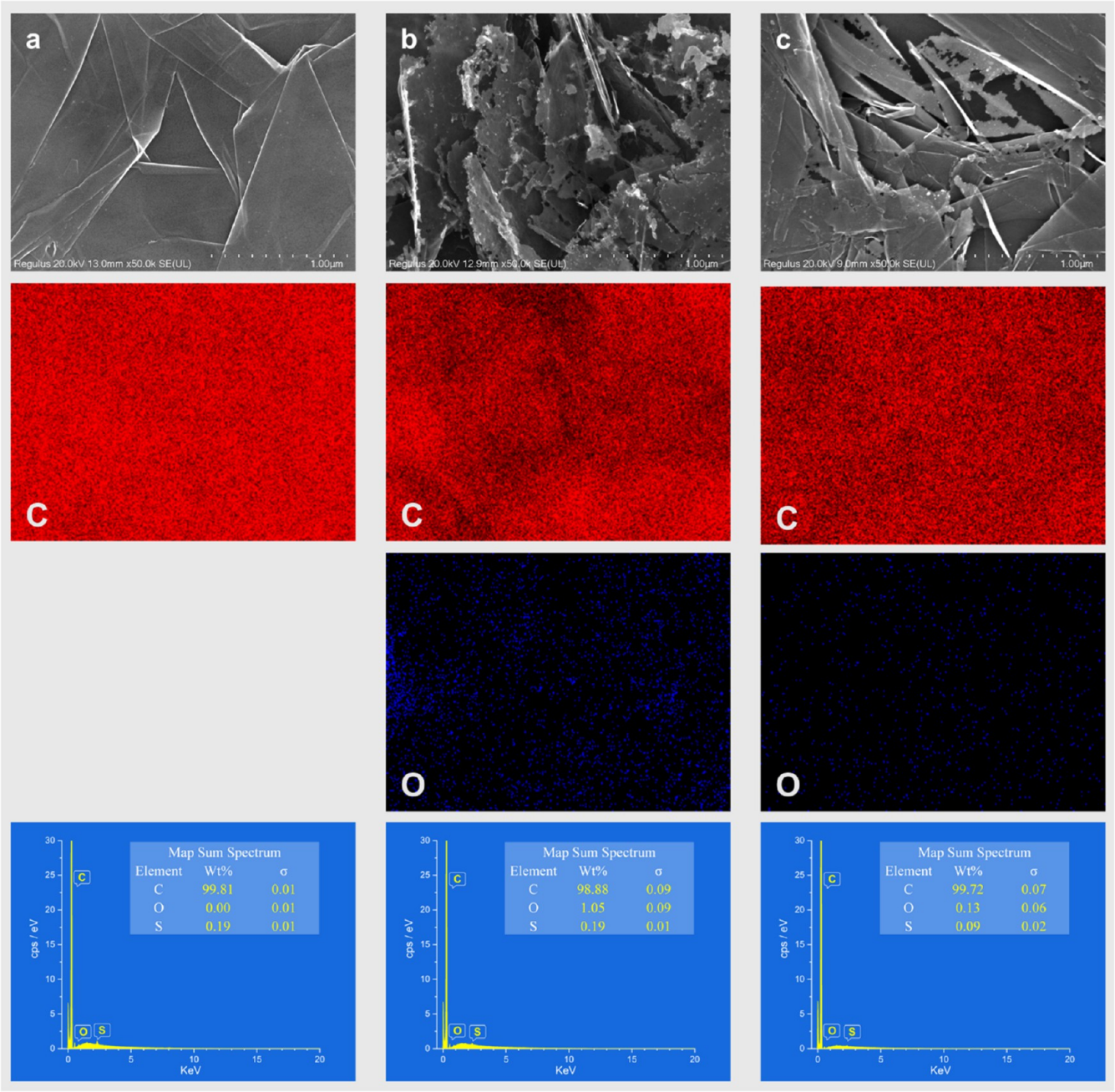

Figure 5. EDS elemental mapping and map sum spectra of (a) MLGD pristine, (b) MLGD-CO_2 MW-PECVD, and (c) MLGD-O_2 MW-PECVD.

the change of intermolecular interactions between the graphene layers and a third part (Figure 6). The PECVD treatment can induce vacancies, voids, and holes in the sample, as well as impurities from the gas composition, which can change the properties, such as resistance and conductivity, and the interaction with chemical species. Figure 5 presents the EDS of MLGD electrodes, indicating the absence of significant impurities from PECVD. It was previously studied that the incorporation of oxygen by PECVD is around 5%; however, it should be noticed that the MLGD-O_2 MW-PECVD (Figure 5c) exhibits oxygen incorporation in located regions, detected around 0.13 wt % along the surface and 1.05 wt % for MLGD-CO_2 MW-PECVD (Figure 5b). Even at higher oxygen doping, no XRD change was detected by PECVD, maintaining the pristine peaks. This low oxygen concentration in graphene samples treated by reactive PECVD proved to be interesting for site activation, resulting in significant improvements in the sensitivity of electrochemical sensors and in the capacitance values of self-supported electrochemical supercapacitors.[47−49] Besides that, since MLGD-O_2 RF-PECVD exhibited a smaller amount of oxygen species presence as MLGD-O_2 microwave-assisted, the type of excitation used to generate the plasma discharge (RF or MW) directs influences in the elemental composition.

An analysis of the effects of different gases used in the MW-PECVD treatment (Figure 6) reveals that the O_2 plasma produces more pronounced edge etching and localized damage (Figure 6c) compared with CO_2 treatment (Figure 6b). However, Raman spectroscopy provides complementary insight showing that the CO_2 plasma leads to a higher I_D/I_G ratio

https://doi.org/10.1021/acsanm.5c03602
ACS Appl. Nano Mater. 2025, 8, 22586−22604

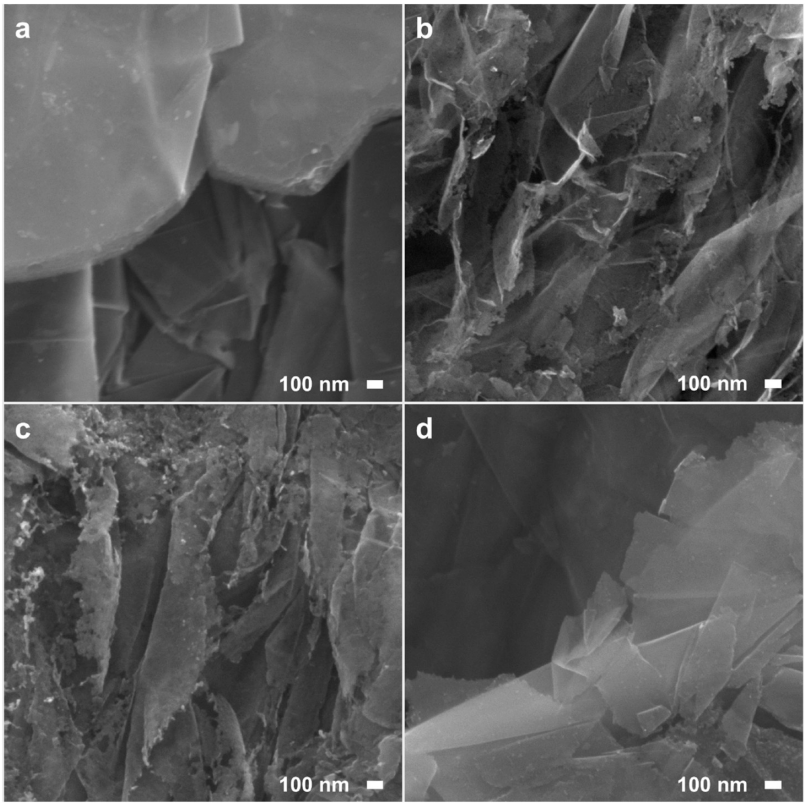

Figure 6. SEM of (a) MLGD pristine, (b) MLGD-CO_2 MW-PECVD, (c) MLGD-O_2 MW-PECVD, and (d) MLGD-O_2 RF-PECVD.

(0.28) than the O_2 MW-PECVD sample (0.26) and the O_2 RF-PECVD sample (0.21) (Figure 4), indicating that CO_2 plasma induces a greater overall defect density across the graphene surface. This apparent contrast between edge morphology and global defect content arises from differences in plasma chemistry and gas-phase energetics: oxygen plasmas possess higher dissociation energy and generate highly reactive O radicals responsible for local edge etching, whereas CO_2 plasmas form a more diverse mixture of CO, O, and OH radicals that promote wider surface oxidation and defect formation over the basal plane.[50,51] These results collectively demonstrate that the type of gas and plasma excitation mode can selectively modulate the balance between edge activation and bulk defect generation, directly influencing the electrochemical behavior of the treated MLGD electrodes. However, PECVD treatment produced localized disruption of the MLG surface (SE-STEM/TEM, Figure 7c) and measurable changes in the near-surface structural order compared to pristine MLGD (Figure 7e). Raman mapping (Figure 4) indicates that no wholesale peak disappearance occurs after plasma exposure, consistent with preservation of the overall sp^2 framework; however, the D-band intensity increases substantially after treatment (I_D/I_G = 0.07 for pristine MLG; 0.28 for CO_2 MW-PECVD; 0.26 for O_2 MW-PECVD; and 0.21 for O_2 RF-PECVD), demonstrating a moderate rise in defect density and edge content. The G-band shows only slight broadening and a small shift, which is consistent with local strain and charge-transfer effects introduced by surface functionalization.[27] Together, the STEM and Raman data indicate that PECVD introduces controlled, edge-localized disorder and oxygenated functionality (holes, vacancies, and edge roughening) while retaining the underlying graphitic lattice, a balance that enhances surface reactivity without causing bulk amorphization. Furthermore, PECVD treatment presented an effect on the surface chemistry by the decreased intensity of high binding energy components, and sp^2/sp^3 hybridization ratio increased, supporting the Raman analysis of a higher I_D/I_G ratio (Figure 4). Plasma exposure alters the near-surface electronic environment of the multilayer graphene electrodes. In this work, the conclusion that the plasma activation modifies the electronic properties of MLG is supported by multiple complementary, indirect observations: (i) Raman spectroscopy shows increased I_D/I_G and slight G-band broadening/shift consistent with enhanced edge/disorder and charge-transfer effects; (ii) EIS data reveal systematic reductions in R_{ct} and increases in conductance after RF-PECVD activation; and (iii) electrochemical behavior (increased capacitance and altered ethanol oxidation currents) consistently reflects an altered density of active electronic states at the electrode surface. These combined indicators are consistent with a plasma-induced shift of the Fermi level and a modification of the effective work function, although no direct photoemission or Kelvin-probe work-function measurement was performed here.[26] Figure 6 shows the SEM images of the MLGD electrodes herein studied. The MLGD pristine (Figure 6a) exhibits a smooth edge and compressed layers. The MW-PECVD (Figure 6b,c) provoked more uniform and dispersed modifications along the surface than RF-PECVD (Figure 6d); however, the latter produced smoother surfaces than the former one as well as preserving the edges of the flakes (Figure 6c). Analyzing the results for samples treated by MW-PECVD, the use of O_2 discharge (Figure 6c) induced higher intense modifications destroying edge layers and producing large holes that mitigate the enhancement produced by PECVDs, due to the new edges having smoother defects than CO_2 discharge (Figure 6b). Therefore, CO_2 MW-PECVD will produce

https://doi.org/10.1021/acsanm.5c03602
ACS Appl. Nano Mater. 2025, 8, 22586−22604

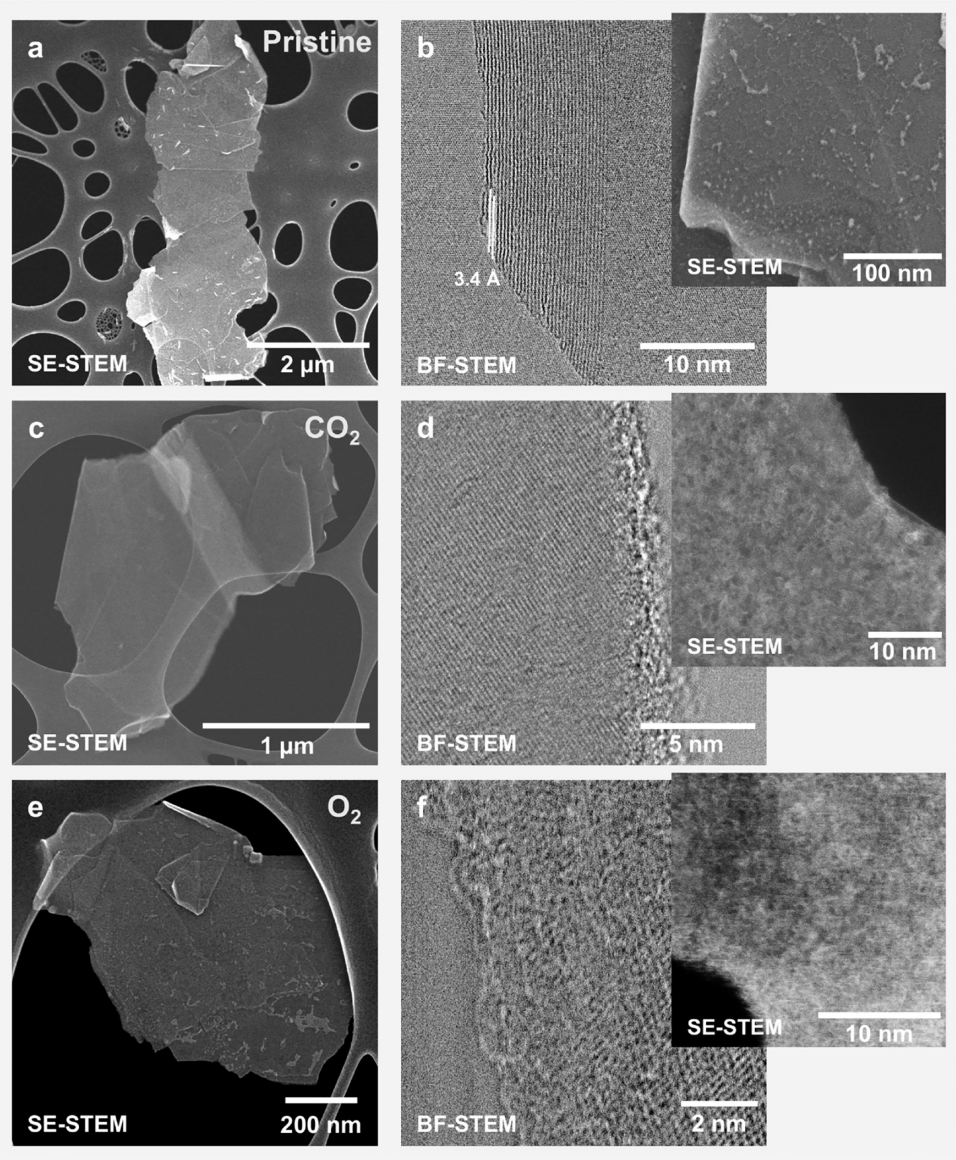

Figure 7. SE-STEM images showing the morphology of (a) pristine, (c) CO_2-treated, and (e) O_2-treated graphene nanomaterials, highlighting their multilayer structure and progressive fragmentation due to oxidation. Corresponding high-resolution BF-STEM images of (b) pristine nanosheets, (d) CO_2-treated graphene, and (f) O_2-treated graphene. Insets show higher-magnification SE-STEM images of the surface and edges, emphasizing the increasing surface roughness from pristine to O_2-treated graphene.

uniform and dispersed edge defects, while O_2 MW-PECVD will produce intense surface modifications, such as large holes and severe destruction of edge sheets, while O_2 RF-PECVD aimed to produce flat and smooth defects in the edges.

Figure 7 shows the secondary electron and bright-field STEM images of graphene nanosheets without (pristine) and with (exposed) CO_2 and O_2 surface treatments. Figure 7a,c,e clearly reveals the multilayer nature of graphene nanomaterials, with pronounced morphological differences depending on the treatment. The pristine nanomaterial (Figures 7a) displays large, thick flakes with well-stacked layers indicative of a highly crystalline structure. In contrast, the CO_2-treated graphene (Figure 7c) shows more delaminated flakes, suggesting partial exfoliation and moderate disruption of the interlayer stacking. The O_2-treated graphene (Figure 7e) features smaller, highly fragmented flakes, pointing to extensive oxidative etching and increased structural disorder. These morphological changes are corroborated by the high-resolution BF-STEM images (Figure 7b,d,f): the pristine graphene exhibits well-defined graphitic fringes with an interlayer spacing of ∼3.4 Å, characteristic of the (002) planes in graphitic materials.[52,53] The CO_2-treated graphene retains some degree of ordering, although signs of surface amorphization are evident at the nanosheet edges. In the case of the O_2-treated graphene, lattice fringes are still present but surrounded by amorphous regions, indicating severe structural degradation. The SE-STEM insets further support this progression, showing smooth surfaces in the pristine material, increased surface roughness in the CO_2-treated graphene, and extensive edge damage and roughening in the O_2-treated counterpart. Altogether, these observations suggest that CO_2 treatment induces moderate structural alterations, whereas exposure to O_2 leads to pronounced oxidative degradation, substantially affecting both the physical structure and potentially the electronic behavior of the graphene.

https://doi.org/10.1021/acsanm.5c03602
ACS Appl. Nano Mater. 2025, 8, 22586−22604

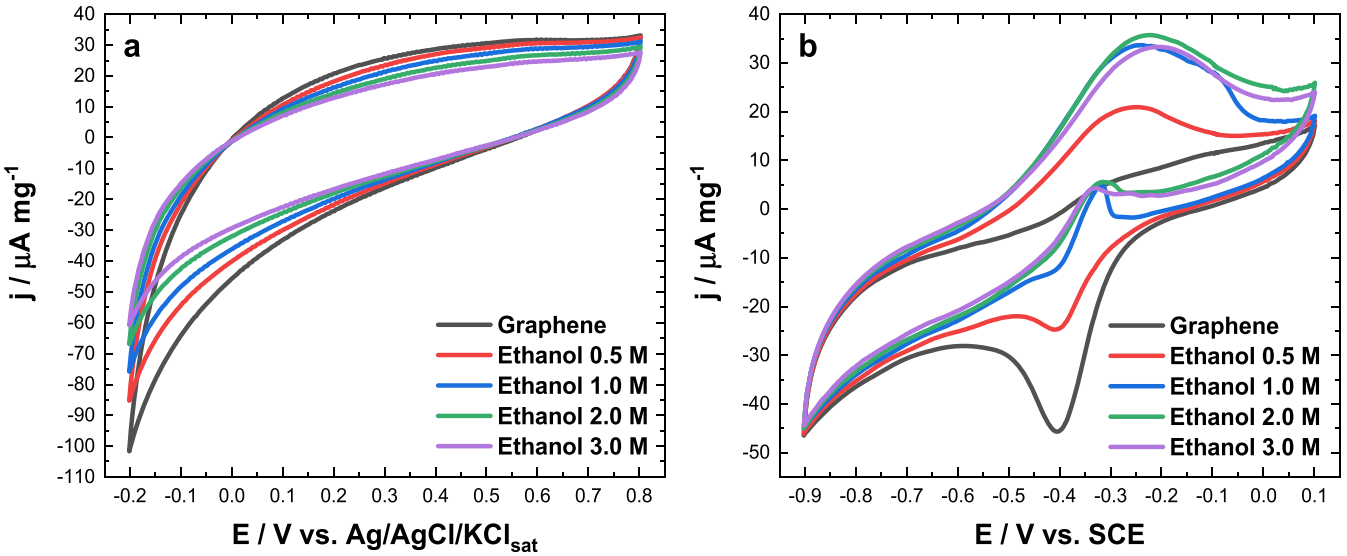

Figure 8. Voltammogram of GP in the electrolyte: (a) 0.5 M H_2SO_4 and (b) 1.0 M NaOH in the oxidation of ethanol at different concentrations, ν = 50 mV S^{1-}.

The morphological differences described in the main text (flake delamination, roughening edge, and local amorphization) are supported quantitatively by the spectroscopic and imaging metrics already presented. First, Raman-derived defect metrics change substantially after PECVD: I_D/I_G increases from 0.07 (pristine) to 0.28 (CO_2 MW-PECVD, a ~4 × increase) and to 0.26 (O_2 MW-PECVD), while the corresponding L_a values drop from ≈275 nm (pristine) to ≈69−74 nm (CO_2/O_2 MW-PECVD). These large fold-changes in I_D/I_G and L_a provide a robust, spatially averaged measure (900-point maps) of increased edge and defect density at the sample surface. Second, EDS elemental mapping shows a markedly higher localized oxygen uptake for CO_2 MW-PECVD (≈1.05 wt % localized O) than for O_2 MW-PECVD (≈0.13 wt % localized O), consistent with CO_2 favoring grafting-type oxygenation, while O_2 produces more etching/fragmentation with less residual surface oxygen. Third, the SEM/STEM micrographs (Figures 6 and 7) show correlated morphological signatures: the CO_2-treated material exhibits more pronounced delaminated/folded regions and increased surface roughness (consistent with increased edge population inferred from I_D/I_G), whereas the O_2-treated material exhibits more extensive local loss of crystalline fringes and hole-like features (consistent with oxidative etching and a higher local amorphous fraction inferred from BF-STEM). Taken together, these complementary, independent metrics (large-area Raman maps, localized EDS quantification, and representative STEM/SEM micrographs) form a coherent quantitative picture: CO_2 MW-PECVD increases near-surface oxygen functionalization and edge population (higher I_D/I_G, higher localized O wt %), while O_2 MW-PECVD produces stronger oxidative fragmentation and local amorphization (loss of lattice fringes and hole formation) even when the residual surface oxygen is lower. The magnitude of the Raman and EDS changes (multifold) and their spatial consistency across the mapped areas support the interpretation that the observed morphological differences between CO_2- and O_2-treated graphene are real and significant within the scope of the presented data set.

To evaluate the direct impact of PECVD treatment on graphene's electrochemical performance, and to explore its future use as a catalyst support in the absence of any metal, we first characterized both pristine graphene powder (GP) and compacted MLG disk electrodes (MLGD) in a standard three-electrode cell. Figure 8 shows cyclic voltammograms of the GP on a glassy-carbon electrode. In both electrolytes, acid and alkaline (Figure 8a,b), the GP (black line) has not presented any electrochemical peak characteristics due to the presence of metals, another indication of the graphene composition purity. The addition of ethanol in H_2SO_4 (Figure 8a) has not shown significant changes, indicating the absence of oxidation activity by GP in acid electrolyte. On the other hand, the areal capacitance was calculated from the CV curve according to the standard method based on the geometric area of the electrode (Figure 8a) and decreases along with the increase of ethanol concentration (Table 1). To facilitate a fair comparison between the two electrode formats, we report complementary normalizations: mass-normalized capacitance (mF/mg) for GP-coated vitreo-carbon electrodes and areal capacitance (mF/cm^2) for compacted MLGD disks. The GP deposits are porous multilayer films formed from a suspension; therefore, mass normalization better reflects the intrinsic charge-storage capacity of the deposited material and its accessible porosity. In contrast, MLGD disks are compacted films with controlled geometry and continuous conductive pathways; areal normalization is therefore more representative of electrode-level performance and practical device metrics. Both normalizations are shown in Table 1.

The presence of ethanol can create diffusional barriers, increasing the interfacial resistance by the change in the viscosity and the conductive environment. Nevertheless, this should affect the capacitance similarly in both electrolytes; the changes in the acid were more intense, while the alkaline electrolytes present a capacitance variation. The higher mobility and protonation of oxygen-containing groups, e.g.,−OH and −COOH, in acid tends to a thinner double layer enhancing the electrostatic interaction leading to a higher capacitance, while in the alkaline electrolyte, OH^- ions along with oxygen-containing groups deprotonated increases the

https://doi.org/10.1021/acsanm.5c03602
ACS Appl. Nano Mater. 2025, 8, 22586−22604

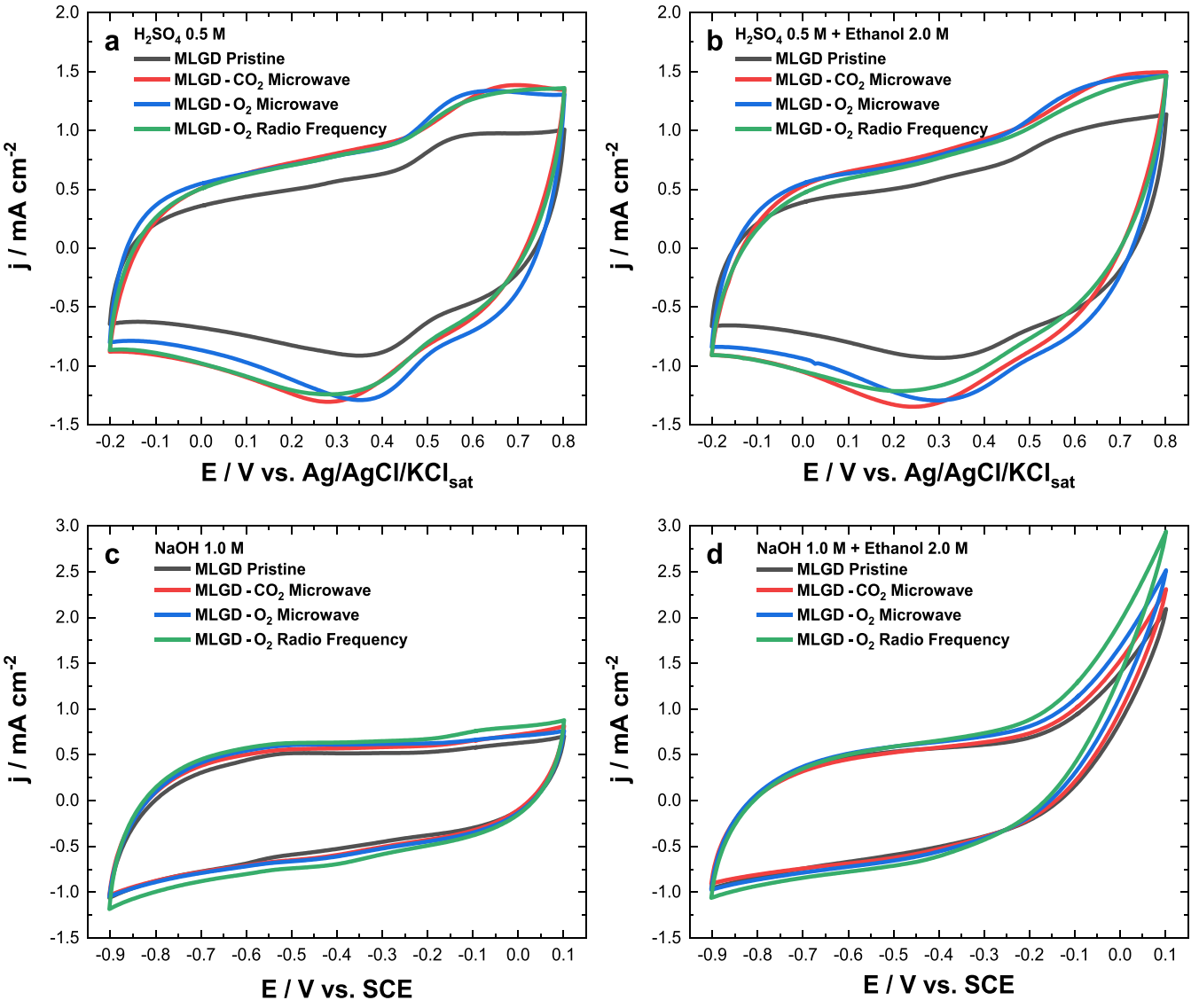

Figure 9. Voltammogram of MLGD electrodes in (a) 0.5 M H_2SO_4, (b) 0.5 M H_2SO_4 + 2.0 M ethanol, (c) 1.0 M NaOH, and (d) 1.0 M NaOH + 2.0 M ethanol, ν = 50 mV S^{1-}.

negative surface charge, expanding the double layer and decreasing the capacitance. Hence, the decrease of capacitance in acid with increase of ethanol concentration is due to the surface charge changes modifying the double layer; while in the alkaline electrolyte, it exhibited a lower capacitance compared with acid, although its surface charges and double layer were more stable.

In the opposite observed during acid voltammograms, in the alkaline electrolyte (Figure 8b), graphene showed catalytic activity in the presence of ethanol, indicating the influence of the OH^- groups present in the solution and the characteristics of the graphene π bonds toward oxidation reactions. Furthermore, the current tends to increase with ethanol concentration up to 1.0 M, beyond which the values at 2.0 M and 3.0 M remain relatively similar, suggesting a plateau. This behavior may be associated with diffusional limitations or changes in interfacial resistance due to ethanol-induced alterations in wettability, which could affect the conductive environment, double-layer structure, and dielectric properties. Notably, the forward and backward scans at 1.0 M show slight differences, indicating possible kinetic or surface interaction effects that are worth further investigation. Electrolyte−material interactions play a decisive role in the catalytic behavior of graphene. In our work, pristine multilayer graphene (GP) already exhibits measurable ethanol oxidation in an alkaline electrolyte, an encouraging result that highlights GP's high surface area and abundant edge sites as intrinsic active centers. Building on this activity, we then move from GP to MLGD to further enhance the current densities and mechanical robustness.

In the acid electrolyte, MLGD have not exhibited ethanol oxidation activity (Figure 9b), and even right after ethanol addition in the solution, the change of voltammogram shape was negligible (individual plots in Figures S1 and S2). Analyzing the impact of plasma treatment on electrochemical performance, the MW-PECVD generated an increase around 35% on catalyst activity, followed by RF-PECVD around 30% (Table 2). In an alkaline electrolyte, the presence of hydroxide ions (OH^-) plays a crucial role in modifying the surface of graphene, toward that, MLGD electrodes in the ethanol solution exhibited oxidation activity (Figure 9d). Furthermore, the edges and defect sites on the electrode structure directly

https://doi.org/10.1021/acsanm.5c03602
ACS Appl. Nano Mater. 2025, 8, 22586−22604

influence oxidation performance, being attested by the increase of the oxidation peaks (0.1 V vs SCE) by the PECVD treatment, where MLGD-O_2 RF-PECVD achieved the highest current density peak (Figure 9d). Compared with acid solution, the performance of MLGD in alkaline pure solution (Figure 9d) exhibited inferior current densities (Table 2); however, paying attention, radiofrequency plasma activation promoted current density peaks 25% and 40% greater than MLGD pristine, in pure and alkaline solutions with ethanol, respectively. The O_2 RF-PECVD treatment produced precise, smooth edge defects (Figure 6d). The zigzag and armchair edges on graphene exhibit different reactivities and electronic states. While zigzag edges can host localized electronic states that may be magnetic, armchair edges generally exhibit different band structures.[54] These edge sites tend to be more reactive than the basal plane due to unsaturated bonds, which increase the susceptibility to chemical modification and increase the reactivity. Zigzag edges are known to present more unsaturated bonds and higher reactivity compared with the basal plane. In our PECVD-treated MLGD samples, evidence for such edge activation is indirect but consistent across multiple techniques: SEM and TEM reveal edge roughening and partial delamination (Figures 6 and 7); Raman spectra (Figure 4) show increased D/G ratios, indicative of a higher defect density; and electrochemical measurements (Tables 2 and 4) display increased double-layer capacitance and ethanol oxidation currents, consistent with a higher population of active edge sites. While XPS with etching and depth profiling would provide quantitative confirmation of the edge versus basal contributions, such experiments are beyond the scope of the present work and will be the subject of future studies. These characteristics, together with the electrolyte and ethanol, demonstrate the efficiency of PECVD treatment in modifying the graphene structure and enhancing its electrochemical activity. The MLGD electrodes capacitance (Table 2) indicated that PECVD increased the surface defects leading to a thinner double layer, producing a higher capacitance in both electrolytes. However, while MLGD-CO_2 and MLGD-O_2 MW-PECVD exhibited the highest capacitance in the acid, an increase of 39% and 34% in comparison to MLGD pristine for electrolyte solution and acid + 2.0 M ethanol, respectively, MLGD-O_2 RF-PECVD performed better in the alkaline electrolyte, indicating that defect produced reacts more effectively with oxygen-containing functional groups improving the electrochemical capacitance and catalytic activity.[50] Taking MLGD pristine as reference, the plasma activation by radiofrequency on graphene surface leads to 27% and 12% increase of capacitance (Table 2) in alkaline solution without and with ethanol presence. Despite the enhanced percentage of capacitance, we should pay attention to the performance of MLGD toward oxidation reactions. GP and MLGD are more electrochemically active in the alkaline electrolytes, and along with RF-PECVD treatment, the MLGD achieved a performance 40% greater than pristine (Table 2).

A comparison between Tables 1 and 2 through complementary normalizations emphasizes different performance aspects: mass-normalized capacitance (mF/mg) for GP-coated glassy-carbon electrodes and areal capacitance (mF/cm^2) for self-supported MLGD disk electrodes (3.0 cm diameter). The GP samples were prepared by drop casting a GP suspension onto a glassy-carbon support (geometric area = 0.385 cm^2); therefore, normalization by deposited mass better reflects the intrinsic charge-storage capacity of the porous multilayer coating and accounts for the role of layer porosity and mass loading in determining the electrochemically accessible surface. In contrast, MLGD disks are compacted, continuous films with substantially higher mass per unit area and a continuous conducting network; areal normalization is therefore the more appropriate metric to evaluate electrode-level behavior and device-relevant performance. Quantitatively, GP deposits show low areal values (≈0.33−0.64 mF/cm^2, Table 1) whereas MLGD disks present much larger areal capacitances (≈11.9−16.8 mF/cm^2, Table 2). This order-of-magnitude difference primarily reflects electrode architecture and mass loading rather than an intrinsic inferiority of the GP material: thin, porous GP coatings have limited mass per area, and their utilization depends strongly on electrolyte penetration, tortuosity, and ion transport within the multilayer. By contrast, MLGD disks provide higher accessible mass and a continuous conductive path, so more surface/defect sites contribute to the measured areal capacitance. PECVD surface modification of MLGD further increases the areal capacitance and ethanol oxidation currents (Table 2), consistent with an increase in electrochemically active sites (defects, edges, oxygen functionalities) that enhance both double-layer and pseudocapacitive contributions and improve reaction kinetics.

Table 3 summarizes the areal capacitances measured at cycles 1, 8, and 15 and the corresponding capacitance-retention values for all MLGD samples (scan rate = 50 mV·s^{-1};

Table 3. Short-Term Cycling Stability Areal Capacitance and Retention Values of MLGD Electrodes

electrode	capacitance (mF/cm^2)			capacitance retention	
	1st cycle	8th cycle	15th cycle	at 8th cycle	at 15th cycle
Acid Electrolyte					
MLGD pristine	11.09	11.73	11.88	105.7%	107.1%
MLGD-CO_2 MW-PECVD	14.99	15.96	16.15	106.5%	107.7%
MLGD-CO_2 MW-PECVD	15.22	16.24	16.52	106.7%	108.6%
MLGD-O_2 RF-PECVD	14.53	15.73	15.98	108.2%	109.9%
Acid Electrolyte + 2.0 M Ethanol					
MLGD pristine	12.50	12.52	12.48	100.1%	99.8%
MLGD-CO_2 MW-PECVD	16.60	16.61	16.58	100.1%	99.9%
MLGD-O_2 MW-PECVD	17.07	16.89	16.76	98.9%	98.2%
MLGD-O_2 RF-PECVD	15.62	15.52	15.46	99.4%	99.0%
Alkaline Electrolyte					
MLGD pristine	8.43	8.86	9.10	105.1%	108.0%
MLGD-CO_2 MW-PECVD	9.15	9.89	10.03	108.1%	109.6%
MLGD-O_2 MW-PECVD	9.39	10.23	10.40	108.9%	110.8%
MLGD-O_2 RF-PECVD	10.79	11.44	11.54	106.0%	106.9%
Alkaline Electrolyte + 2.0 M Ethanol					
MLGD pristine	8.94	8.90	8.85	99.5%	99.0%
MLGD-CO_2 MW-PECVD	8.86	8.99	8.92	101.4%	100.6%
MLGD-O_2 MW-PECVD	9.73	9.61	9.53	98.8%	98.0%
MLGD-O_2 RF-PECVD	10.42	10.11	9.95	97.1%	95.6%

https://doi.org/10.1021/acsanm.5c03602
ACS Appl. Nano Mater. 2025, 8, 22586−22604

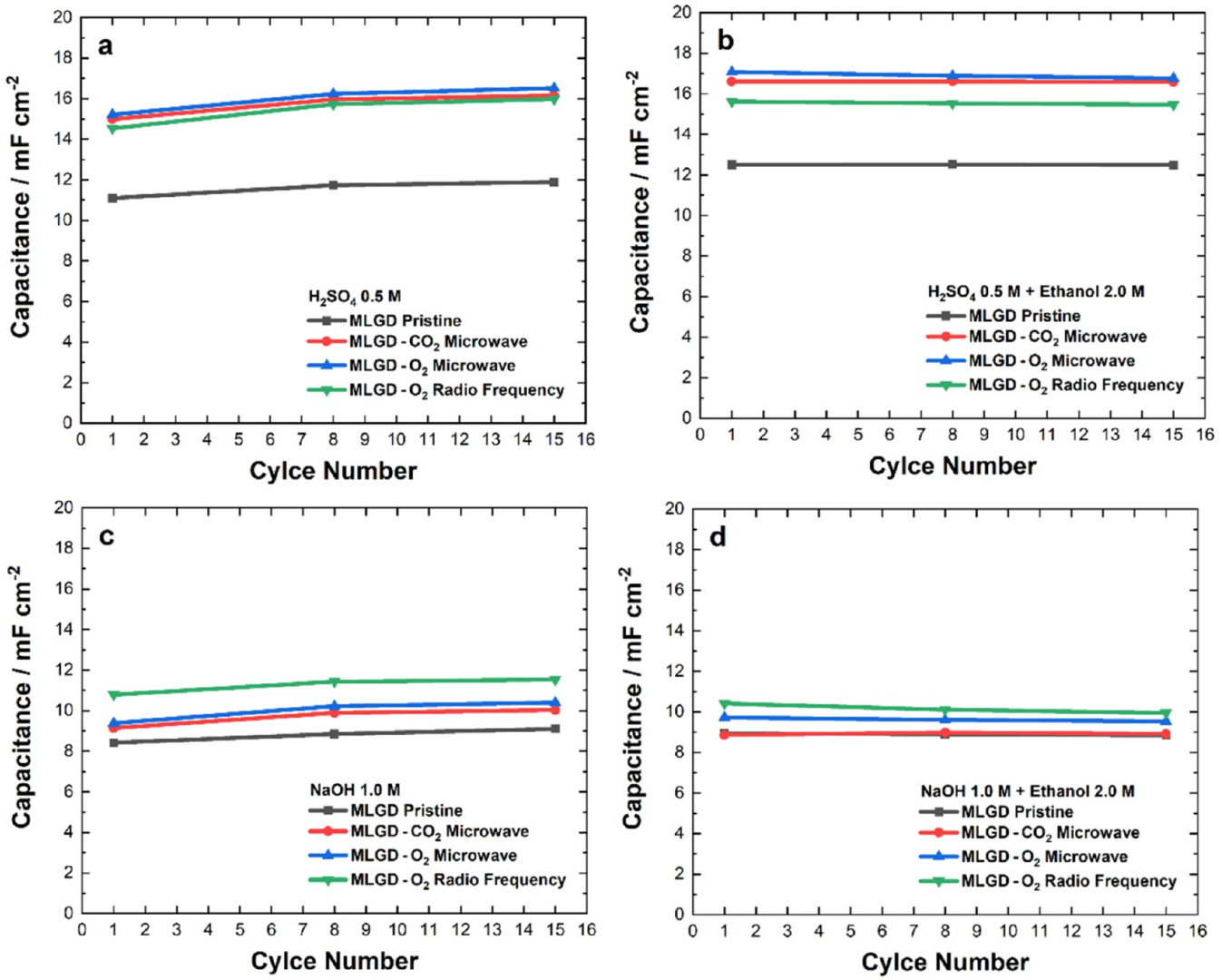

Figure 10. Capacitance-retention plots of MLGD electrodes over 15 consecutive CV cycles in different solutions: (a) 0.5 M H_2SO_4, (b) 0.5 M H_2SO_4 + 2.0 M ethanol, (c) 1.0 M NaOH, and (d) 1.0 M NaOH + 2.0 M ethanol.

capacitance calculated from Figure 9). The data show excellent short-term stability for all electrodes: retention after 15 cycles ranges from 95.6% to 110.8%, with most samples exhibiting >98% retention. In acid electrolytes, the PECVD-treated MLGD electrodes display modest increases in areal capacitance over the first 15 cycles (up to ≈ 110% for O_2 RF-PECVD), which we attribute to a short activation/wetting stage (progressive electrolyte penetration, exposure of near-surface defect sites, and removal of weakly adsorbed species) rather than to irreversible structural changes. In acid + 2.0 M ethanol, the areal capacitances remain essentially unchanged (≈99−100% retention), indicating that ethanol at this concentration does not induce short-term degradation. In alkaline electrolytes, the treated disks again show small conditioning increases (≈106−111% retention for several PECVD samples), whereas in alkaline + ethanol, a few electrodes show slight decreases (down to 95.6% for O_2 RF-PECVD), likely reflecting competitive adsorption of organic species and subtle changes in ion access under these conditions.

Figure 10 presents the capacitance-retention plots derived from the tabulated data (percent retention vs cycle number), which provides a compact visual summary of the numerical trends reported in Table 3. Representative CV overlays are provided in Figures S3−S6; the overlays confirm negligible change in voltametric shape between the first and 15th cycles. Taken together, the quantitative retention plots, numeric table, and stacked CVs demonstrate stable short-term electrochemical behavior of the MLGD electrodes under the tested conditions. Extended long-term durability (e.g., accelerated cycling to thousands of cycles or extended chronoamperometry) is beyond the scope of the present work and will be addressed in future studies.

The areal capacitances measured for our compacted MLGD disk electrodes (≈11.9−16.8 mF·cm^{-2}; Table 2) are comparable to values reported for simple graphene films and coated electrodes in three-electrode CV measurements, although they are lower than values published for purposely engineered 3D or hybrid electrodes that maximize mass loading and ionic accessibility. For context, prior studies report areal capacitances of the same order of magnitude for thin graphene coatings (e.g., ∼7.7 mF·cm^{-2} in coated 2D electrodes and ∼22.5 mF·cm^{-2} for optimized drop-cast/rGO films), whereas vertically aligned, foam-like or thick binder-free 3D

https://doi.org/10.1021/acsanm.5c03602
ACS Appl. Nano Mater. 2025, 8, 22586−22604

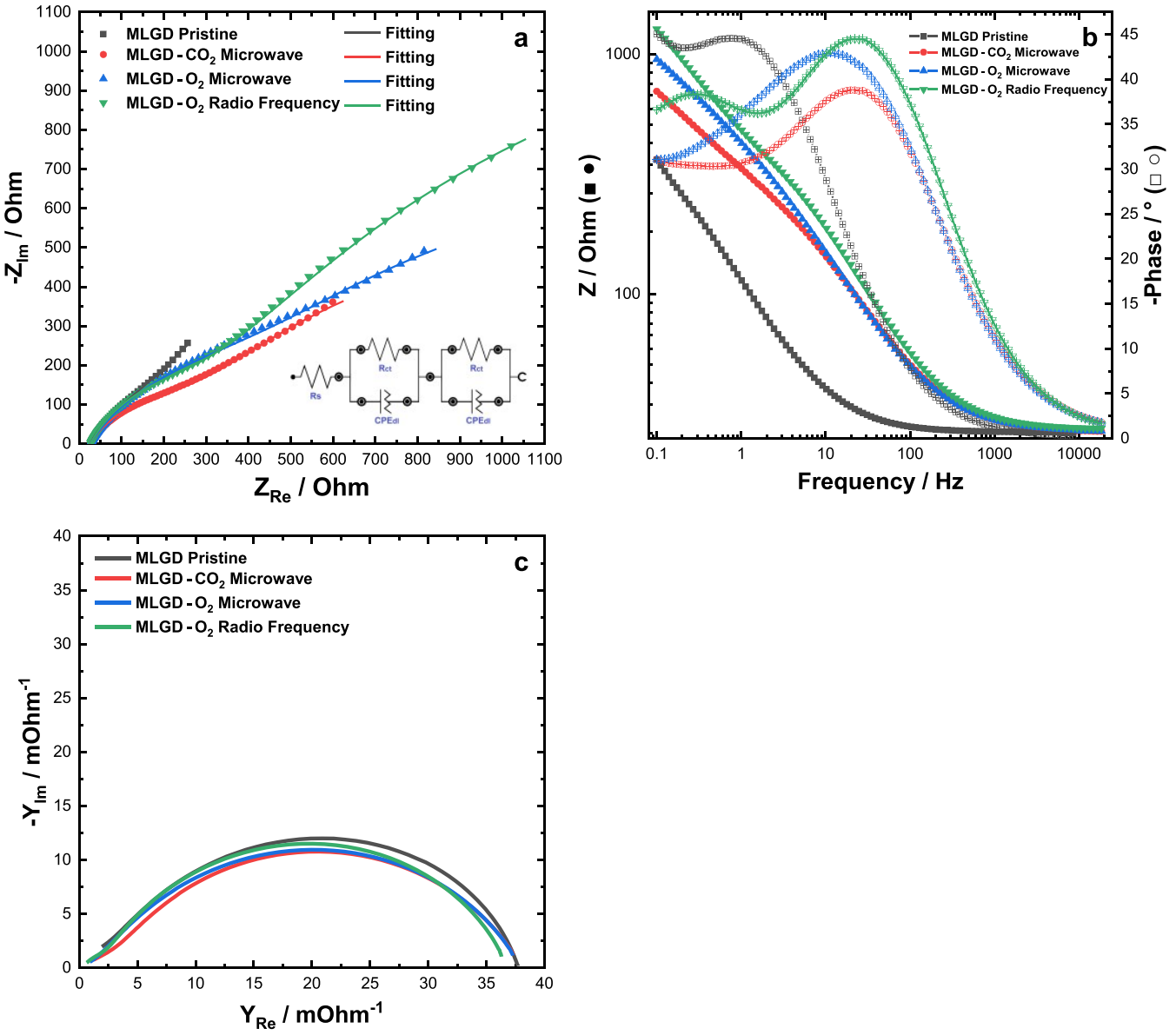

Figure 11. Nyquist impedance spectra plot with its respective fit (solid line) (a), Bode plots of the impedance magnitude (b), and Nyquist admittance (c) of MLGD electrodes without catalyst ink in 0.1 M KOH, E = 0.1 V vs Ag/AgCl/KClsat, frequency range of 50 kHz to 1 mHz, using an AC amplitude of 1 mV p/p.

architectures can deliver areal capacitances in the hundreds to thousands of mF·cm^{-2} range.[55,56] Several factors account for these differences. First, areal capacitance scales strongly with accessible mass per unit area and with the electrode's pore architecture: 3D scaffolds and thick binder-free films concurrently maximize accessible area and ion pathways and therefore give much larger areal values than thin or simply compacted disks. Second, chemical activation, heteroatom doping, or inclusion of redox-active additives increase both gravimetric and areal capacitances and are absent in the present MLGD disks. Third, measurement conditions (scan rate, electrolyte type and concentration, and three-electrode geometry) influence measured values; higher scan rates generally reduce the measured capacitance, while alkaline versus acidic media change double-layer and pseudocapacitive contributions. Importantly, despite the moderate absolute values, PECVD surface modification consistently increases the areal capacitance of MLGD relative to pristine disks (Table 2), indicating that surface defectivity and oxygen functionalities enhanced electrochemical accessibility and charge storage in our system. We therefore conclude that the measured capacitances are reasonable for the electrode format studied and that the PECVD treatment produces a meaningful and reproducible improvement in electrochemical performance.[57,58]

The electrooxidation of ethanol proceeds through complex pathways that depend strongly on the electrolyte environment. In an acidic electrolyte, partial oxidation typically yields acetaldehyde and acetic acid as the dominant products, with full C−C bond cleavage to CO_2 being kinetically limited at low temperatures.[59,60] In an alkaline electrolyte, the reaction is facilitated by the availability of OH^- species, and the main products are acetaldehyde and acetate, again with only limited CO_2 generation.[61,62] Product selectivity and the relative contribution of these parallel pathways are known to depend on the electrode material, defect density, and local surface

https://doi.org/10.1021/acsanm.5c03602
ACS Appl. Nano Mater. 2025, 8, 22586−22604

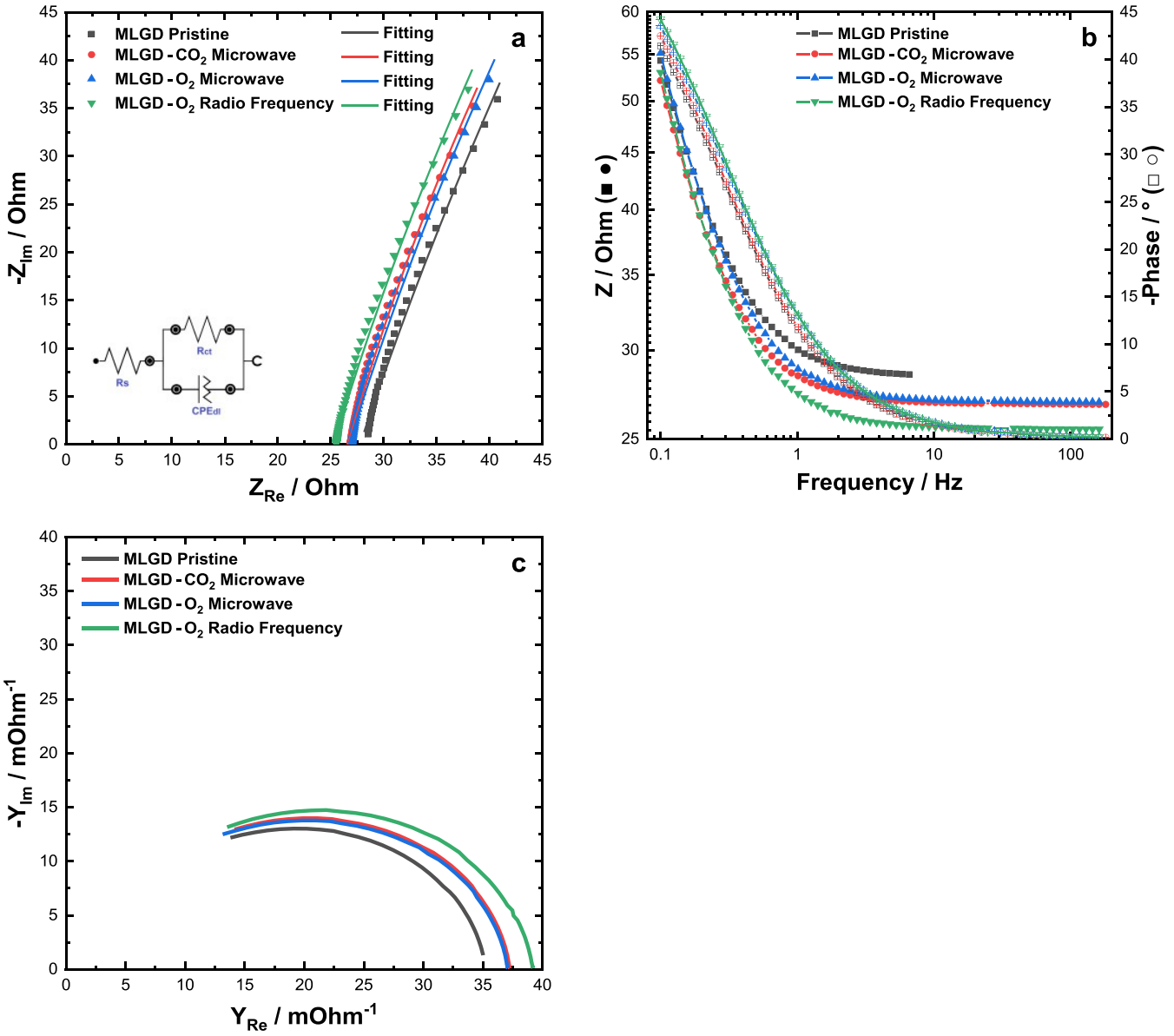

Figure 12. Nyquist impedance spectra plot with its respective fit (solid line) (a), Bode plots of the impedance magnitude (b), and Nyquist admittance (c) of MLGD electrodes with catalyst ink in 0.1 M KOH, E = 0.1 V vs Ag/AgCl/KClsat, frequency range of 50 kHz to 1 mHz, using an AC amplitude of 1 mV p/p.

chemistry. In our study, ethanol served as a molecular probe to evaluate the impact of PECVD surface activation on graphene activity and we did not carry out quantitative product analysis. Therefore, rigorous product and intermediate identification will be required to directly correlate PECVD-induced defect structures to product distributions.

Figures 11 and 12 show the EIS Nyquist plots, Bode magnitude plots, and admittance representations for MLGD electrodes without and with catalyst ink, respectively. The equivalent circuits used for fitting are Randles-type models augmented with constant phase elements to account for the nonideal double-layer behavior. In these circuits, Rs is the solution resistance, R_{ct} the charge-transfer resistance related to electron transfer during ethanol oxidation, and the CPE (CPEdl) models the nonideal double layer (see Experimental Section).[63] Fit quality (χ^2) is summarized in Table 4 and demonstrates that the selected circuits describe the data within an acceptable error.

In the Nyquist plots (Figure 11a), the high-frequency semicircle is assigned to charge transfer, while the low-frequency inclined line is associated with mass transport/diffusion. For several pristine MLGD electrodes, the semicircle does not close fully at low frequency, and the response is better captured by a two-RC (two interface) model: one R_{ct}–CPE pair representing the electrode–electrolyte outer interface (double layer and immediate charge transfer) and a second R_{ct}–CPE pair describing additional interfacial/bulk processes (subsurface porosity, internal contacts, and defect-related sites). The two-RC model yields lower χ^2 and smaller fit residuals than a single-RC model for these electrodes, indicating that it more accurately represents the distinct electrochemical processes present (see Table 4 and Supporting Information). In contrast, ink-sprayed electrodes are well-described by a single-RC model because the catalyst ink homogenizes the surface and merges the two contributions into a single dominant interfacial response.

https://doi.org/10.1021/acsanm.5c03602
ACS Appl. Nano Mater. 2025, 8, 22586–22604

Table 4. Electrochemical Impedance Spectroscopy of MGLD Electrodes Calculated from Figures 11 and 12

		1st RC interface		2nd RC interface			
electrode	R_s (Ω)	R_{ct} (Ω)	CPE_{dl} (mF)	R_{ct} (Ω)	CPE_{dl} (mF)	Y_{real} (mΩ)	χ^2
Electrode without Catalyst Ink							
MLGD pristine	26.20	158.16	2.88	2093.60	11.74	37.69	0.0181
MLGD-CO_2 MW-PECVD	26.01	1829.40	4.57	206.05	0.17	37.32	0.0118
MLGD-O_2 MW-PECVD	25.99	2042.50	3.07	376.60	0.27	37.29	0.0108
MLGD-O_2 RF-PECVD	26.81	235.48	0.12	3493.50	1.85	36.30	0.0076
Electrode with Catalyst Ink							
MLGD pristine	27.76	875.08	79.70			35.01	0.0071
MLGD-CO_2 MW-PECVD	26.63	567.79	66.14			37.26	0.0103
MLGD-O_2 MW-PECVD	26.71	725.64	67.06			37.08	0.0128
MLGD-O_2 RF-PECVD	25.29	697.93	67.50			39.20	0.0112

PECVD treatment alters both the capacitive and resistive properties. For bare MLGD, O_2-PECVD increases the CPE magnitude (Y_0) and the derived C_{eff}, consistent with an increase in electrochemically accessible surface area due to more edges/defects; however, excessive defecting can also increase charge-carrier scattering and raise effective R_{ct} or reduce Y_{real}. For ink-sprayed electrodes, PECVD improves catalyst−electrode coupling and reduces R_{ct}. MW-PECVD produced an ≈6% increase in conductance relative to pristine, while RF-PECVD produced ∼12% improvement (Table 4), consistent with the enhanced ethanol oxidation currents observed by CV. The diagonal curvature in the low-frequency region of the Nyquist plots suggests minor diffusion limitations under the present experimental conditions, which are reinforced by scan-rate CV analysis (Figure 9). Together, the EIS and CV results show that PECVD increases electrochemical activity via increased active site density, while the net effect on charge transport depends on the balance between the added active sites and defect-induced scattering.

Finally, increasing the ethanol concentration leads to modest decreases in areal capacitance and slight increases in interfacial resistance. EIS fits show systematic changes in CPE parameters (Y_0 and n) with ethanol content, indicating altered ion accessibility and double-layer formation consistent with a partial diffusional barrier introduced by adsorbed organic species (Table 4). These observations do not indicate catastrophic electrode degradation; rather, they reflect interfacial modulation by ethanol that is reproducible across samples.

Plasma-enhanced chemical vapor deposition (PECVD) was used here as a post-treatment to introduce controlled edge defects and oxygenated functional groups on preformed MLG disk electrodes. Compared with common wet chemical oxidation (e.g., Hummers-type) or liquid chemical functionalization, PECVD provides several practical advantages: (i) dry, reagent-free processing that avoids chemical contamination and hazardous wastes; (ii) rapid treatment times (MW-PECVD: 2 min; RF-PECVD: 25 min per side in our conditions) enabling high throughput; (iii) tunable surface chemistry via choice of feed gas, pressure, and excitation mode (Ar/CO_2 vs Ar/O_2; MW vs RF) for controlled defect density and oxygen incorporation; (iv) uniform, reproducible surface activation across disk electrodes suitable for batch processing; and (v) minimal impact on bulk crystallinity as seen by XRD while producing the desirable increase in electrochemical activity and capacitance (Tables 2 and 4). In our experiments, EDS mapping indicated low overall contamination after PECVD (MLGD-CO_2 MW-PECVD: ≈1.05 wt % O in localized regions; MLGD-O_2 MW-PECVD: ≈0.13 wt % O), Raman, and STEM show controlled edge disorder rather than wholesale amorphization (see Figures 4 and 7), and EIS/CV data show increased capacitance and up to 40% enhancement in ethanol oxidation peak current for specific PECVD conditions (MLGD-O_2 RF-PECVD). For these reasons, we present PECVD as a practical, fast, and clean postfunctionalization route when the objective is to tune surface-active sites on multilayer graphene supports rather than to synthesize monolayer graphene or to perform wet chemical functionalization. Compared with wet chemical oxidation and laser-induced graphene approaches, PECVD offers rapid, reagent-free functionalization with tunable defect density and minimal contamination. A comparative overview of the main features of these approaches is summarized in Table S1. Although PECVD systems require capital investment, the plasma activation used here is a fast, dry, and reagent-free surface functionalization route that (a) avoids hazardous wet chemistries, (b) yields reproducible surface modification across disks, and (c) may scale to batch processing of multiple disks with relatively low per-sample consumable cost compared with that of wet chemical functionalization. For these reasons, we present PECVD as a practical post-treatment when the objective is clean, rapid surface activation rather than large-area monolayer growth.[64,65]

CONCLUSION

This study demonstrates a scalable route to produce self-supported multilayer graphene disk (MLGD) electrodes by exfoliation of thermally expanded graphite, followed by plasma-enhanced chemical vapor deposition (PECVD) activation. The process combines high-yield graphene synthesis with rapid, solvent-free surface modification, enabling tunable control of the defect density and oxygen functionality while preserving bulk crystallinity. Raman mapping confirmed a controlled rise in disorder (I_D/I_G from 0.07 in pristine MLG to 0.26−0.28 after PECVD) and reduced crystallite sizes (L_a ≈ 69−92 nm), consistent with selective edge activation. EDS analysis revealed localized oxygen incorporation (≈1.05 wt % for CO_2 MW vs ≈0.13 wt % for O_2 MW), correlating with distinct plasma chemistries. Morphological analyses showed that CO_2 plasma promotes edge delamination, while O_2 induces localized fragmentation. These structural and chemical modifications led to higher double-layer capacitance and up to ≈40% enhancement in ethanol oxidation peak current, with stable cycling performance. Overall, PECVD post-treatment of compacted MLG electrodes offers a rapid, clean, and reproducible strategy to engineer electroactive carbon

https://doi.org/10.1021/acsanm.5c03602
ACS Appl. Nano Mater. 2025, 8, 22586−22604

supports. Future work will apply microscale in situ techniques (DEMS, ATR-FTIR, online GC/HPLC) to correlate plasma-induced surface chemistry with product selectivity, building on this foundation toward application in anion-exchange membrane fuel cells.

■ ASSOCIATED CONTENT

Supporting Information

The Supporting Information is available free of charge at https://pubs.acs.org/doi/10.1021/acsanm.5c03602.

Cyclic voltammetry stability tests of MLGD electrodes comparing electrolytes with and without ethanol in both acidic and alkaline media (Figures S1−S6); 3D electrochemical impedance spectroscopy (EIS) analyses of MLGD electrodes, recorded with and without catalyst ink, displaying the complex-plane (Nyquist) and Bode plots in 0.1 M KOH at 0.1 V vs Ag/AgCl/KCl_sat over the 50 kHz−1 mHz frequency range (AC amplitude 0.1 mV p−p) (Figures S7 and S8); and comparative summary of surface functionalization and fabrication approaches relevant to MLG disk electrodes (Table S1) (PDF)

■ AUTHOR INFORMATION

Corresponding Author

Flavio Colmati − *Institute of Chemistry, Federal University of Goiás, 74690-900 Goiânia, GO, Brazil; Center of Excellence in Hydrogen and Sustainable Energy Technologies (CEHTES), 74690-631 Goiânia, GO, Brazil;* orcid.org/0000-0002-1867-0091; Email: colmati@ufg.br

Authors

Tarso Leandro Bastos − *Institute of Chemistry, Federal University of Goiás, 74690-900 Goiânia, GO, Brazil; CENIMAT|i3N, Department of Materials Science, School of Science and Technology, NOVA University Lisbon and CEMOP/UNINOVA, 2829-516 Caparica, Portugal; Center of Excellence in Hydrogen and Sustainable Energy Technologies (CEHTES), 74690-631 Goiânia, GO, Brazil;* orcid.org/0000-0002-2357-3149

Camila Cristina da Silva − *Institute of Technological and Exact Sciences, Federal University of Triângulo Mineiro, 38025-180 Uberaba, MG, Brazil*

Daniela Nunes − *CENIMAT|i3N, Department of Materials Science, School of Science and Technology, NOVA University Lisbon and CEMOP/UNINOVA, 2829-516 Caparica, Portugal*

Elvira Fortunato − *CENIMAT|i3N, Department of Materials Science, School of Science and Technology, NOVA University Lisbon and CEMOP/UNINOVA, 2829-516 Caparica, Portugal*

Rodrigo Martins − *CENIMAT|i3N, Department of Materials Science, School of Science and Technology, NOVA University Lisbon and CEMOP/UNINOVA, 2829-516 Caparica, Portugal*

Devadharshini Kathan − *Department of Chemical Engineering, University of South Carolina, Columbia, South Carolina 29208, United States*

William Earl Mustain, Jr − *Department of Chemical Engineering, University of South Carolina, Columbia, South Carolina 29208, United States;* orcid.org/0000-0001-7804-6410

Rogério Valentim Gelamo − *Institute of Technological and Exact Sciences, Federal University of Triângulo Mineiro, 38025-180 Uberaba, MG, Brazil;* orcid.org/0000-0003-2124-3450

Complete contact information is available at: https://pubs.acs.org/10.1021/acsanm.5c03602

Author Contributions

T.B.: writing—original draft, methodology, formal analysis, data curation, conceptualization; C.S.: investigation; D.N., E.F., and R.M.: writing—review and editing, formal analysis, data curation; D.K.: formal analysis, investigation; W.M.: writing—review and editing, resources, conceptualization; R.G.: writing—review and editing, resources, supervision, methodology, conceptualization; F.C.: writing—review and editing, supervision, methodology, conceptualization.

Funding

The Article Processing Charge for the publication of this research was funded by the Coordenacao de Aperfeicoamento de Pessoal de Nivel Superior (CAPES), Brazil (ROR identifier: 00x0ma614).

Notes

The authors declare no competing financial interest.

■ ACKNOWLEDGMENTS

T.L.B. thanks Capes for Scholarships 88887.701552/2022-00 and 88881.933962/2024-01. F.C. thanks CNPq, Grant 405793/2022-7, and FAPEG Grant 202110267000537. R.V.G. thanks CNPq, Grant 302582/2021-5, Fapemig, Grant APQ-05247-23, and the Brazilian Institute of Science and Technology (INCT) in Carbon Nanomaterials and Nacional de Grafite Ltda. National Funds from FCT—Fundação para a Ciência e a Tecnologia, I.P., supported this work through Projects UIDB/50025/2020-2023, UIDP/50025/2020-2023, and LA/0037/2020 of the Associate Laboratory Institute of Nanostructures, Nanomodelling and Nanofabrication-i3N. We are thankful to the Sustainable Stone Project by Portugal—Valorization of Natural Stone for a digital, sustainable, and qualified future, numbered 40, proposal number C644943391-00000051, which is cofinanced by the PRR—Recovery and Resilience Plan of the European Union (Next Generation EU). The authors acknowledge the financial support for Open Access provided by CAPES, under the agreement between CAPES and the American Chemical Society, order number 10000989064.

■ REFERENCES

(1) de Souza Augusto, G.; Scarmínio, J.; Catarini Silva, P. R.; de Siervo, A.; Rout, C. S.; Rouxinol, F.; Gelamo, R. V. Flexible Metal-Free Supercapacitors Based on Multilayer Graphene Electrodes. *Electrochim. Acta* **2018**, *285*, 241−253.

(2) Pereira, J. F. S.; Di-Oliveira, M.; Faria, L. V.; Borges, P. H. S.; Nossol, E.; Gelamo, R. V.; Richter, E. M.; Lopes, O. F.; Muñoz, R. A. A. CO2-Plasma Surface Treatment of Graphite Sheet Electrodes for Detection of Chloramphenicol, Ciprofloxacin and Sulphanilamide. *Microchim. Acta* **2023**, *190* (10), 379.

(3) Gürünlü, B.; Taşdelen-Yücedağ, Ç.; Bayramoğlu, M. Graphene Synthesis by Ultrasound Energy-Assisted Exfoliation of Graphite in Various Solvents. *Crystals* **2020**, *10* (11), No. 1037.

(4) Novoselov, K. S.; Geim, A. K.; Morozov, S. V.; Jiang, D.; Zhang, Y.; Dubonos, S. V.; Grigorieva, I. V.; Firsov, A. A. Electric Field Effect in Atomically Thin Carbon Films. *Science* **2004**, *306* (5696), 666−669.

(5) Dato, A.; Radmilovic, V.; Lee, Z.; Phillips, J.; Frenklach, M. Substrate-Free Gas-Phase Synthesis of Graphene Sheets. *Nano Lett.* **2008**, *8* (7), 2012−2016.
(6) Lu, C.-H.; Hao, D.; Yeh, N.-C. A Perspective of Recent Advances in PECVD-Grown Graphene Thin Films for Scientific Research and Technological Applications. *Mater. Chem. Phys.* **2024**, *319*, No. 129318.
(7) Boaretti, C.; Roso, M.; Bonora, R.; Modesti, M.; Lorenzetti, A. Investigation of Plasma-Assisted Functionalization of Graphitic Materials for Epoxy Composites. *Nanomaterials* **2020**, *10* (1), No. 78.
(8) Bertran-Serra, E.; Rodriguez-Miguel, S.; Li, Z.; Ma, Y.; Farid, G.; Chaitoglou, S.; Amade, R.; Ospina, R.; Andújar, J.-L. Advancements in Plasma-Enhanced Chemical Vapor Deposition for Producing Vertical Graphene Nanowalls. *Nanomaterials* **2023**, *13* (18), No. 2533.
(9) Alsagri, M.; Laref, A.; Ul Haq, B.; AlQahtani, H. R.; Nya, F. T.; El Amine Monir, M.; Chowdhury, S.; Alghamdi, E. A.; Huang, H. M.; Yang, J. T.; Xiong, Y. C. The Effect of Non-Metals (O, F) Dopant on the Electronic Structure, Dirac Cone, and Optical Characteristics of Graphene Sheets Applicable for Gas Sensing. *J. Mol. Struct.* **2024**, *1299*, No. 137102.
(10) Kemp, M. Low Temperature Plasma Process Effectively Modifies Surface of Graphene. *AM&P Techn. Articles* **2014**, *172* (11), 15−18.
(11) Li, M.; Liu, D.; Wei, D.; Song, X.; Wei, D.; Wee, A. T. S. Controllable Synthesis of Graphene by Plasma-Enhanced Chemical Vapor Deposition and Its Related Applications. *Adv. Sci.* **2016**, *3* (11), No. 1600003.
(12) Boyd, D. A.; Lin, W.-H.; Hsu, C.-C.; Teague, M. L.; Chen, C.-C.; Lo, Y.-Y.; Chan, W.-Y.; Su, W.-B.; Cheng, T.-C.; Chang, C.-S.; Wu, C.-I.; Yeh, N.-C. Single-Step Deposition of High-Mobility Graphene at Reduced Temperatures. *Nat. Commun.* **2015**, *6* (1), No. 6620.
(13) Pereira, J. F. S.; Borges, P. H. S.; Moura, G. M.; Gelamo, R. V.; Nossol, E.; Canobre, S. C.; Richter, E. M.; Munoz, R. A. A. Improved Electrochemical Performance of Pyrolytic Graphite Paper: Electrochemical versus Reactive Cold-Plasma Activation. *Electrochem. Commun.* **2019**, *105*, No. 106497.
(14) Pereira, J. F. S.; Rocha, R. G.; Castro, S. V. F.; João, A. F.; Borges, P. H. S.; Rocha, D. P.; de Siervo, A.; Richter, E. M.; Nossol, E.; Gelamo, R. V.; Muñoz, R. A. A. Reactive Oxygen Plasma Treatment of 3D-Printed Carbon Electrodes towards High-Performance Electrochemical Sensors. *Sens. Actuators, B* **2021**, *347*, No. 130651.
(15) McAllister, M. J.; Li, J.-L.; Adamson, D. H.; Schniepp, H. C.; Abdala, A. A.; Liu, J.; Herrera-Alonso, M.; Milius, D. L.; Car, R.; Prud'homme, R. K.; Aksay, I. A. Single Sheet Functionalized Graphene by Oxidation and Thermal Expansion of Graphite. *Chem. Mater.* **2007**, *19* (18), 4396−4404.
(16) Pereira, J. F. S.; Melo, L. M. A.; Arantes, L. C.; Borges, P. H. S.; Faria, L. V.; da Cunha, K. F.; Souza, K. A. O.; Soté, W. O.; Costa, J. L.; Nossol, E.; Gelamo, R. V.; Richter, E. M.; Comar, M.; dos Santos, W. T. P.; Lopes, O. F.; Muñoz, R. A. A. Oxygen Plasma-Treated Graphite Sheet Electrodes: A Sensitive and Disposable Sensor for Methamphetamines. *Electrochim. Acta* **2023**, *467*, No. 143089.
(17) de Moraes Moura, G.; da Silva, C. C.; Naves, E. A. A.; Moreto, J. A.; Ferreira, D. C.; de Oliveira, P. R.; Kalinke, C.; Scarminio, J.; de Siervo, A.; da Cunha, T. H. R.; Gelamo, R. V. On the Physical and Electrochemical Properties of MLG-Based Electrode Surfaces Modified by Microwave-Assisted Reactive Plasma. *Mater. Sci. Eng. B* **2021**, *272*, No. 115346.
(18) Cai, W.; Lai, T.; Du, H.; Ye, J. Electrochemical Determination of Ascorbic Acid, Dopamine and Uric Acid Based on an Exfoliated Graphite Paper Electrode: A High Performance Flexible Sensor. *Sens Actuators, B* **2014**, *193*, 492−500.
(19) Chee, W. K.; Lim, H. N.; Zainal, Z.; Huang, N. M.; Harrison, I.; Andou, Y. Flexible Graphene-Based Supercapacitors: A Review. *J. Phys. Chem. C* **2016**, *120* (8), 4153−4172.
(20) Ehsani, A.; Heidari, A. A.; Asgari, R. Electrocatalytic Oxidation of Ethanol on the Surface of Graphene Based Nanocomposites: An Introduction and Review to It in Recent Studies. *Chem. Rec.* **2019**, *19* (11), 2341−2360.
(21) Xie, J.; Sun, X.; Zhang, N.; Xu, K.; Zhou, M.; Xie, Y. Layer-by-Layer β-Ni(OH)2/Graphene Nanohybrids for Ultraflexible All-Solid-State Thin-Film Supercapacitors with High Electrochemical Performance. *Nano Energy* **2013**, *2* (1), 65−74.
(22) Bastos, T. L.; da Silva, C. C.; Cui, Y.; Al Murisi, M.; Amirsalehi, M.; Biancolli, A. L. G.; Varcoe, J. R.; Gelamo, R. V.; Mustain, W. E.; Colmati, F. Application of Multi-Layer Graphene (MLG) in the Anion Exchange Membrane Fuel Cells. *J. Power Sources* **2025**, *660*, No. 238558.
(23) Haruna, A.; Dönmez, K. B.; Hooshmand, S.; Avcı, E.; Qamar, M.; Zaidi, S. A.; Shahzad, F.; Miller, T. S.; Chakrabarti, B. K.; Howard, C. A.; Bayazıt, M. K. Harmony of Nanosystems: Graphitic Carbon Nitride/Carbon Nanomaterial Hybrid Architectures for Energy Storage in Supercapacitors and Batteries. *Carbon* **2024**, *226*, No. 119177.
(24) Mishra, Y.; Chattaraj, A.; Aljabali, A. A.; El-Tanani, M.; Tambuwala, M. M.; Mishra, V. Graphene Oxide−Lithium-Ion Batteries: Inauguration of an Era in Energy Storage Technology. *Clean Energy* **2024**, *8* (3), 194−205.
(25) Machuno, L. G. B.; Oliveira, A. R.; Furlan, R. H.; Lima, A. B.; Morais, L. C.; Gelamo, R. V. Multilayer Graphene Films Obtained by Dip Coating Technique. *Mater. Res.* **2015**, *18* (4), 775−780.
(26) Patil, U. V.; Pawbake, A. S.; Machuno, L. G. B.; Gelamo, R. V.; Jadkar, S. R.; Rout, C. S.; Late, D. J. Effect of Plasma Treatment on Multilayer Graphene: X-Ray Photoelectron Spectroscopy, Surface Morphology Investigations and Work Function Measurements. *RSC Adv.* **2016**, *6* (54), 48843−48850.
(27) Khare, R. T.; Gelamo, R. V.; More, M. A.; Late, D. J.; Rout, C. S. Enhanced Field Emission of Plasma Treated Multilayer Graphene. *Appl. Phys. Lett.* **2015**, *107* (12), No. 123503.
(28) Gelamo, R. V.; Durrant, S. F.; Trasferetti, B. C.; Davanzo, C. U.; Rouxinol, F. P. M.; Bica de Moraes, M. A. Helium Ion Irradiation of Polymer Films Deposited from TMS-Ar Plasmas. *Plasma Processes Polym.* **2007**, *4* (4), 489−496.
(29) Cançado, L. G.; Jorio, A.; Ferreira, E. H. M.; Stavale, F.; Achete, C. A.; Capaz, R. B.; Moutinho, M. V. O.; Lombardo, A.; Kulmala, T. S.; Ferrari, A. C. Quantifying Defects in Graphene via Raman Spectroscopy at Different Excitation Energies. *Nano Lett.* **2011**, *11* (8), 3190−3196.
(30) Yaqoob, L.; Noor, T.; Iqbal, N. A Comprehensive and Critical Review of the Recent Progress in Electrocatalysts for the Ethanol Oxidation Reaction. *RSC Adv.* **2021**, *11* (27), 16768−16804.
(31) Altarawneh, R. M.; Majidi, P.; Pickup, P. G. Determination of the Efficiency of Ethanol Oxidation in a Proton Exchange Membrane Electrolysis Cell. *J. Power Sources* **2017**, *351*, 106−114.
(32) Peng, B.; Yan, Y.-G.; Cai, W.-B. Surface-Enhanced IR Spectroscopy Investigation on the Electro-Oxidation of CO Adlayer at a Polycrystalline Pt Film Electrode in Cl−-Containing HClO4. *Electrochim. Acta* **2010**, *55* (27), 8307−8311.
(33) Bastos, T. L.; Gelamo, R. V.; Colmati, F. Carbon-Graphene Hybrid Supporting Platinum−Tin Electrocatalyst to Enhance Ethanol Oxidation Reaction. *J. Appl. Electrochem.* **2024**, *54*, 1225−1237.
(34) Bastos, T. L.; Gelamo, R. V.; Colmati, F. Multi-Layer Graphene Powder (without Metal Nanoparticles) Booster Carbon Supported Platinum-Tin Electrocatalyst for the Ethanol Oxidation Reactions. *Next Mater.* **2025**, *8*, No. 100807.
(35) Bastos, T. L.; Gelamo, R. V.; Colmati, F. The Influence of Carbon Spheres and Graphene Synthesized by Thermal Method as Platinum-Tin Electrocatalyst Supports to Enhance the Ethanol Oxidation. *J. Solid State Electrochem.* **2025**, *29*, 1079−1092.
(36) Daş, E.; Kaplan, B. Y.; Gürsel, S. A.; Yurtcan, A. B. Graphene Nanoplatelets-Carbon Black Hybrids as an Efficient Catalyst Support for Pt Nanoparticles for Polymer Electrolyte Membrane Fuel Cells. *Renewable Energy* **2019**, *139*, 1099−1110.
(37) Wu, G.; More, K. L.; Xu, P.; Wang, H.-L.; Ferrandon, M.; Kropf, A. J.; Myers, D. J.; Ma, S.; Johnston, C. M.; Zelenay, P. A Carbon-Nanotube-Supported Graphene-Rich Non-Precious Metal

https://doi.org/10.1021/acsanm.5c03602
ACS Appl. Nano Mater. 2025, 8, 22586−22604

Oxygen Reduction Catalyst with Enhanced Performance Durability. *Chem. Commun.* **2013**, *49* (32), 3291.
(38) Cao, A.; Xu, C.; Liang, J.; Wu, D.; Wei, B. X-Ray Diffraction Characterization on the Alignment Degree of Carbon Nanotubes. *Chem. Phys. Lett.* **2001**, *344* (1−2), 13−17.
(39) Wang, Y.; Panzik, J. E.; Kiefer, B.; Lee, K. K. M. Crystal Structure of Graphite under Room-Temperature Compression and Decompression. *Sci. Rep.* **2012**, *2* (1), No. 520.
(40) Warren, B. E. X-Ray Diffraction in Random Layer Lattices. *Phys. Rev.* **1941**, *59* (9), 693−698.
(41) Li, Z. Q.; Lu, C. J.; Xia, Z. P.; Zhou, Y.; Luo, Z. X-Ray Diffraction Patterns of Graphite and Turbostratic Carbon. *Carbon* **2007**, *45* (8), 1686−1695.
(42) Some, S.; Kim, Y.; Yoon, Y.; Yoo, H.; Lee, S.; Park, Y.; Lee, H. High-Quality Reduced Graphene Oxide by a Dual-Function Chemical Reduction and Healing Process. *Sci. Rep* **2013**, *3* (1), No. 1929.
(43) Storm, M. M.; Johnsen, R. E.; Norby, P. In Situ X-Ray Powder Diffraction Studies of the Synthesis of Graphene Oxide and Formation of Reduced Graphene Oxide. *J. Solid State Chem.* **2016**, *240*, 49−54.
(44) Johnson, R.; Zafar, M. A.; Thomas, S.; Jacob, M. V. A Critical Review on Vacuum and Atmospheric Microwave Plasma-Based Graphene Synthesis. *FlatChem* **2025**, *50*, No. 100812.
(45) Ferrari, A. C.; Robertson, J. Interpretation of Raman Spectra of Disordered and Amorphous Carbon. *Phys. Rev. B* **2000**, *61* (20), No. 14095.
(46) *Plasma Deposition, Treatment, and Etching of Polymers*; d'Agostino, R., Ed.; Academic Press:: Boston, 1990.
(47) de Moraes Moura, G.; da Silva, C. C.; Naves, E. A. A.; Moreto, J. A.; Ferreira, D. C.; de Oliveira, P. R.; Kalinke, C.; Scarminio, J.; de Siervo, A.; da Cunha, T. H. R.; Gelamo, R. V. On the Physical and Electrochemical Properties of MLG-based Electrode Surfaces Modified by Microwave-Assisted Reactive Plasma. *Mater. Sci. Eng. B* **2021**, *272*, No. 115346.
(48) Moreto, J. A.; Silva, P. H. S.; de Moraes Moura, G.; da Silva, C. C.; Ferreira, D. C.; da Cunha, T. H. R.; Silva, G. G.; Rouxinol, F.; de Siervo, A.; Gelamo, R. V. The Effect of Plasma Treatment on Flexible Self-Standing Supercapacitors Composed by Carbon Nanotubes and Multilayer Graphene Composites. *J. Mater. Sci.* **2022**, *57* (19), 8779−8799.
(49) Pereira, J. F. S.; Melo, L. M. A.; Arantes, L. C.; Borges, P. H. S.; Faria, L. V.; da Cunha, K. F.; Souza, K. A. O.; Soté, W. O.; Costa, J. L.; Nossol, E.; Gelamo, R. V.; Richter, E. M.; Comar, M.; dos Santos, W. T. P.; Lopes, O. F.; Muñoz, R. A. A. Oxygen Plasma-treated Graphite Sheet Electrodes: A Sensitive and Disposable Sensor for Methamphetamines. *Electrochim. Acta* **2023**, *467*, No. 143089.
(50) Ahmed, N.; Luo, W.; Zhao, R.; Zhang, Q.; Wu, D.; Zheng, X.; Wang, H.; Cui, C. Role of Plasma in Catalyst Preparation and Modification for Oxygen Evolution Reaction. *Precis. Chem.* **2025**, *3*, 110−127.
(51) Gelamo, R. V.; Durrant, S. F.; Trasferetti, B. C.; Davanzo, C. U.; Rouxinol, F. P. M.; Bica de Moraes, M. A. Helium ion Irradiation of Polymer Films Deposited from TMS-Ar Plasmas. *Plasma Processes Polym.* **2007**, *4* (4), 489−496.
(52) Islam, F.; Tahmasebi, A.; Moghtaderi, B.; Yu, J. Structural Investigation of the Synthesized Few-Layer Graphene from Coal under Microwave. *Nanomaterials* **2022**, *12* (1), No. 57.
(53) Lin, W. M.; Suresh, G.; Gupta, V. P.; Tomida, S.; Oyama, K.; Yaakob, Y.; Asaka, T.; Sonoyama, N.; Yusop, M. Z. M.; Tanemura, M. In Situ Transmission Electron Microscopy Observation of Electrochemical Process Between Li−C Nanocomposites and Multilayer Graphene. *Adv. Mater. Technol.* **2024**, *9* (5), No. 2301564.
(54) Lado, J. L.; García-Martínez, N.; Fernández-Rossier, J. Edge States in Graphene-like Systems. *Synth. Met.* **2015**, *210*, 56−67.
(55) Islam, M. R.; Afroj, S.; Karim, N. Scalable Production of 2D Material Heterostructure Textiles for High-Performance Wearable Supercapacitors. *ACS Nano* **2023**, *17* (18), 18481−18493.
(56) Mishukova, V.; Boulanger, N.; Iakunkov, A.; Delekta, S. S.; Zhuang, X.; Talyzin, A.; Li, J. Facile Fabrication of Graphene-Based High-Performance Microsupercapacitors Operating at a High Temperature of 150 °C. *Nanoscale Adv.* **2021**, *3* (16), 4674−4679.
(57) Ke, Q.; Wang, J. Graphene-Based Materials for Supercapacitor Electrodes − A Review. *J. Materiomics* **2016**, *2* (1), 37−54.
(58) Le Fevre, L. W.; Cao, J.; Kinloch, I. A.; Forsyth, A. J.; Dryfe, R. A. W. Systematic Comparison of Graphene Materials for Supercapacitor Electrodes. *ChemistryOpen* **2019**, *8* (4), 418−428.
(59) de Souza, J. P. I.; Queiroz, S. L.; Bergamaski, K.; Gonzalez, E. R.; Nart, F. C. Electro-Oxidation of Ethanol on Pt, Rh, and PtRh Electrodes. A Study Using DEMS and in-Situ FTIR Techniques. *J. Phys. Chem. B* **2002**, *106* (38), 9825−9830.
(60) Heinen, M.; Jusys, Z.; Behm, R. J. Ethanol, Acetaldehyde and Acetic Acid Adsorption/Electrooxidation on a Pt Thin Film Electrode under Continuous Electrolyte Flow: An in Situ ATR-FTIRS Flow Cell Study. *J. Phys. Chem. C* **2010**, *114* (21), 9850−9864.
(61) Fontes, E. H.; Piasentin, R. M.; Ayoub, J. M. S.; da Silva, J. C. M.; Assumpção, M. H. M. T.; Spinacé, E. V.; Neto, A. O.; de Souza, R. F. B. Electrochemical and in Situ ATR-FTIR Studies of Ethanol Electro-Oxidation in Alkaline Medium Using PtRh/C Electrocatalysts. *Mater. Renewable Sustainable Energy* **2015**, *4* (1), No. 3.
(62) Kaur, J.; Gupta, R. K.; Kumar, A. Electrocatalytic Ethanol Oxidation Reaction: Recent Progress, Challenges, and Future Prospects. *Discover Nano* **2024**, *19* (1), No. 137.
(63) Xu, Z.; Zhang, Q.; Ji, Q.; Gao, X.; Chen, G.; Xie, S.; Cai, G.; Shen, Y.; Chen, L.; Sun, J.; Yang, Z.; Chen, L.; Cheng, Y.-J.; Müller-Buschbaum, P.; Xia, Y. Facile Scalable Multilevel Structure Engineering Makes Ti0.667Nb1.333O4 a New Promising Lithium-Ion Battery Anode. *Mater. Today Sustainability* **2023**, *24*, No. 100521.
(64) MOOSA, A. A.; ABED, M. S. Graphene Preparation and Graphite Exfoliation. *Turk J. Chem.* **2021**, *45* (3), 493−519.
(65) Melero, C.; Rincón, R.; Muñoz, J.; Zhang, G.; Sun, S.; Perez, A.; Royuela, O.; González-Gago, C.; Calzada, M. D. Scalable Graphene Production from Ethanol Decomposition by Microwave Argon Plasma Torch. *Plasma Phys. Controlled Fusion* **2018**, *60* (1), No. 014009.

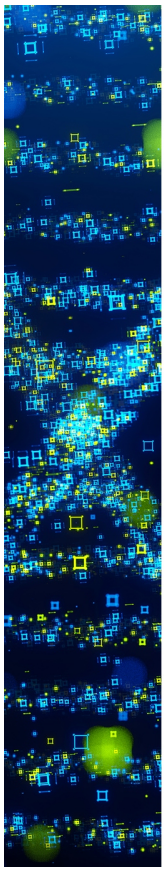

https://doi.org/10.1021/acsanm.5c03602
ACS Appl. Nano Mater. 2025, 8, 22586−22604